JGR Oceans

RESEARCH ARTICLE
10.1029/2020JC017146

Brazil Current Volume Transport Variability During 2009–2015 From a Long-Term Moored Array at 34.5°S

M. P. Chidichimo[1,2,3], A. R. Piola[1,2,3,4], C. S. Meinen[5], R. C. Perez[5], E. J. D. Campos[6,7], S. Dong[5], R. Lumpkin[5], and S. L. Garzoli[5]

[1]Departamento de Oceanografía, Servicio de Hidrografía Naval, Buenos Aires, Argentina, [2]Consejo Nacional de Investigaciones Científicas y Técnicas (CONICET), Buenos Aires, Argentina, [3]CNRS – IRD – CONICET UBA, Instituto Franco-Argentino para el Estudio del Clima y sus Impactos (UMI 3351 IFAECI), Buenos Aires, Argentina, [4]Universidad de Buenos Aires, Buenos Aires, Argentina, [5]National Oceanic and Atmospheric Administration, Atlantic Oceanographic and Meteorological Laboratory, Miami, FL, USA, [6]Oceanographic Institute of the University of Sao Paulo, São Paulo, Brazil, [7]Department of Biology, Chemistry, and Environmental Sciences, College of Arts and Sciences, American University of Sharjah, Sharjah, United Arab Emirates

Key Points:

- The multiyear continuous absolute Brazil Current transport measured at 34.5°S has significant variability on daily to monthly time scales
- The baroclinic component accounts for the largest part of the absolute transport variance, but the barotropic variance is not negligible
- No meaningful seasonal cycle, interannual variability, or trend is detected during the roughly 6 years of daily transport measurements

Correspondence to:
M. P. Chidichimo,
mpchidichimo@hidro.gov.ar

Citation:
Chidichimo, M. P., Piola, A. R., Meinen, C. S., Perez, R. C., Campos, E. J. D., Dong, S., et al. (2021). Brazil Current volume transport variability during 2009–2015 from a long-term moored array at 34.5°S. *Journal of Geophysical Research: Oceans*, *126*, e2020JC017146. https://doi.org/10.1029/2020JC017146

Received 29 DEC 2020
Accepted 1 APR 2021

Abstract The Brazil Current, the western limb of the subtropical gyre of the South Atlantic Ocean, is one of the major Western Boundary Currents of the global ocean. Here, we present the first multiyear continuous daily time series of Brazil Current absolute volume transport obtained using 6+ years of observations from a line of four pressure-recording inverted echo sounders (PIES) deployed at 34.5°S. The array was augmented in December 2012 with two current meter-equipped PIES and in December 2013 with a moored Acoustic Doppler Current Profiler on the upper continental slope. The Brazil Current is bounded by the sea surface and the neutral density interface separating South Atlantic Central Water and Antarctic Intermediate Water, which is on average at a reference pressure of 628 ± 46 dbar, and it is confined west of 49.5°W. The Brazil Current has a mean strength of −14.0 ± 2.8 Sv (1 Sv ≡ 10^6 m^3 s^{-1}; negative indicates southward flow) with a temporal standard deviation of 8.8 Sv and peak-to-peak range from −41.7 to +20 Sv. About 80% of the absolute transport variance is concentrated at periods shorter than 150 days with a prominent peak at 100 days. The baroclinic component accounts for 85% of the absolute transport variance, but the barotropic variance is not negligible. The baroclinic and barotropic transports are uncorrelated, demonstrating the need to measure both transport components independently. Given the energetic high frequency transport variations, statistically significant seasonal to interannual variability and trends have yet to be detected.

Plain Language Summary Western Boundary Currents are the most intense currents of the global ocean and are key to the redistribution of mass, heat, salt, and carbon throughout the globe. In the South Atlantic, the Brazil Current transports warm and salty waters off the South American coast toward the pole and is a major driver of climate variability. This study presents, for the first time, multiyear continuous-in-time direct observations of the Brazil Current at 34.5°S. Roughly 6 years of daily measurements from moored sensors, together with high-resolution snapshots of temperature, salinity, oxygen, and velocity collected during seven oceanographic cruises since 2009, provide the ability to characterize the daily to seasonal to year-to-year variability of the Brazil Current with unprecedented detail. These observations reveal strong and rapid changes in the Brazil Current on time scales as short as 14–60 days, allow quantification of the required sampling to resolve longer-term variability, and improve estimates of the Brazil Current transport. The Brazil Current variability is dominated by the east-west density variations in the water column although east-west differences in bottom pressure are not negligible. Understanding of the strength, structure, and time variability of the Brazil Current is needed to improve model representations of this important flow.

1. Introduction

The Brazil Current (BC) is one of the major Western Boundary Currents (WBCs). WBCs are essential components of the ocean circulation and understanding their short-term and long-term variability and the mechanisms that drive them is a fundamental element of oceanic and climate research (e.g., Archer et al., 2018; Imawaki et al., 2013; Palmer et al., 2019; Todd et al., 2019). While the existence of the BC has

been known for nearly two centuries (e.g., Rennell, 1832), and the mean circulation patterns of the current have been understood for several decades (e.g., Peterson & Stramma, 1991; Stramma et al., 1990), there are still many open questions about the temporal variability of the BC and the mechanisms that drive those variations.

The southward flowing BC is the western limb of the subtropical gyre of the South Atlantic Ocean, carrying relatively warm and salty waters along the continental margin of eastern South America. The BC originates in the subtropics between roughly 10° and 15°S where the westward flowing trans-Atlantic South Equatorial Current bifurcates (e.g., Rodrigues et al., 2007; Stramma, 1991; Stramma et al., 1990) in two branches: The northern branch forms the North Brazil Current and the southern branch forms the BC. After the bifurcation, the BC flows southward along the continental margin of South America, slowly increasing its southward time-mean transport from −0.8 Sv near 10°–25°S to −70 Sv at roughly 35°–38°S (negative transport indicates southward flow), attributed in part due to a tight anticyclonic recirculation cell in the southwest South Atlantic to the east of the mean BC flow in the upper 1,400 m (e.g., Peterson & Stramma, 1991; Stramma et al., 1990). At 36°–38°S, it encounters the northward flowing cold and fresh waters of the Malvinas Current, a northward branch of the Antarctic Circumpolar Current (e.g., Ferrari et al., 2017; Spadone & Provost, 2009; Vivier & Provost, 1999) and forms the Brazil-Malvinas Confluence (BMC), which meanders off toward the east (e.g., Gordon & Greengrove, 1986; Lumpkin & Garzoli, 2011; Olson et al., 1988). Along its southward path, the BC is located mostly over the upper continental margin, with mesoscale features impacting its mean flow and producing occasional separations from the shelf break (e.g., Calado et al., 2010; Campos et al., 2000; Lima et al., 2016; Soutelino et al., 2011). It has been reported that the BC separates from the shelf break for the last time at about 36°S (Goni et al., 2011; Olson et al., 1988).

Most of the available historical estimates of the southward BC transport are geostrophic relative to pre-defined levels of no motion and are based on hydrographic observations collected in the 1980s and 1990s between 12° and 25°S (see Peterson & Stramma, 1991). Around 20°S, the BC is located close to the continental shelf, with values around −6 Sv (e.g., Peterson & Stramma, 1991; Stramma et al., 1990). Historical estimates of BC transport near 23°S to 24°S have varied from −13.2 to −4.1 Sv (Campos et al., 1995; Garfield, 1990; Stramma, 1989; Zemba, 1991). More recently, geostrophic estimates from historical ship data yielded a mean transport of −5.6 Sv above 500 m at 23°–26°S (Biló et al., 2014). Near 33°–35°S, the historical hydrographic transports are typically around −24 to −18 Sv (Boebel et al., 1999; Garzoli et al., 1993; Olson et al., 1988; Peterson & Stramma, 1991).

A few historical continuous-in-time mooring records of the BC variability do exist, although in most cases the records are short (only a few months). These historical time series generally did not include the barotropic component of the flow. Müller et al. (1998) provided the sole historical transport time series observations to directly observe the flow over the Brazilian continental slope using nearly two-year long current-meter mooring arrays between 20° and 28°S. They observed a southward deepening and strengthening of the BC, reaching down to 670 m at 28°S with a transport of −16 Sv west of 45°W. Several studies have quantified the baroclinic transport component using Inverted Echo Sounders (IES) between 35° and 38°, finding time-mean transports of −24 to −10 Sv above 800 m over time periods of 15 and 8 months, respectively (Confluence Principal Investigators, 1990; Garzoli, 1993; Garzoli & Bianchi, 1987; Garzoli & Garraffo, 1989; Garzoli & Simionato, 1990). Although other studies based on repeated expendable bathythermograph (XBT) transects (e.g., Garzoli & Baringer, 2007; Garzoli et al., 2013; Goes et al., 2019; Lima et al., 2016), surface drifters (Oliveira et al., 2009), combined hydrographic data and quasi-isobaric subsurface floats (Rodrigues et al., 2010), satellite altimetry and temperature data (Goni et al., 2011; Goni, Bringas, & DiNezio, 2011), blended products with satellite altimetry and winds (Lumpkin & Garzoli, 2011), or on combinations of Argo floats and satellite altimetry (Schmid, 2014; Schmid & Majumder, 2018) have revealed some aspects of the BC time-mean and temporal variability, they were limited either in their spatial and/or temporal coverage. As a result, much remains unknown about the spatial structure of the BC and how it varies across a range of time scales.

There is great interest in observing the BC at 34.5°S, as at this latitude the BC is close to its transport maximum based on the limited observations to date at that latitude (e.g., Garzoli, 1993; Peterson & Stramma, 1991; Stramma, 1989). Furthermore, on the large-scale context, this latitude marks the entrance to the subtropical South Atlantic, as it corresponds to the southern boundary of the African continent. For this

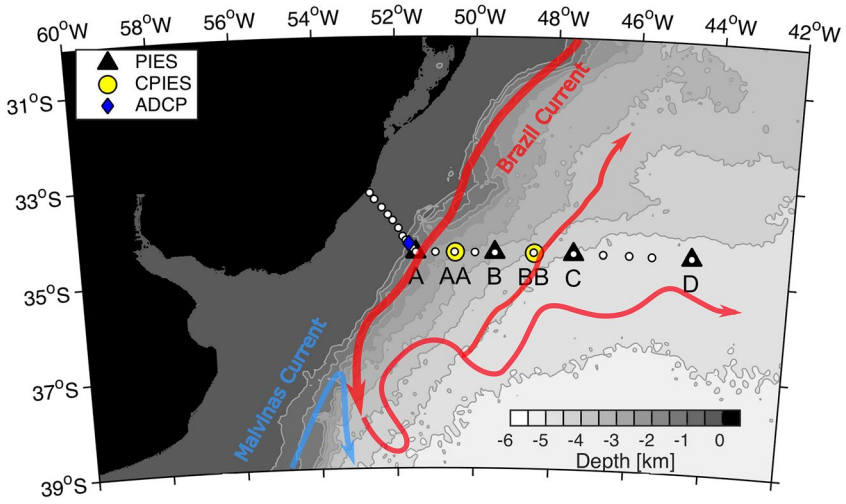

Figure 1. Configuration of the SAMBA-West array: PIES (black triangles), CPIES (yellow circles), ADCP mooring (blue diamond). PIES/CPIES site names on the transport line are displayed. White circles represent the nominal positions of the hydrographic CTD/O_2/LADCP stations (Table 2). Bathymetry (shaded background) comes from the Smith and Sandwell (1997) data set. The arrows on top represent the surface and sub-surface circulation of the Brazil Current (red) and Malvinas Current (light blue) based on the climatological time-mean dynamic topography (1993–2012) extracted from https://www.aviso.altimetry.fr/. CPIES, current- and pressure-recording inverted echo sounder; CTD, conductivity, temperature, and depth; LADCP, Lowered Acoustic Doppler Current Profiler; PIES, pressure-recording inverted echo sounder; SAMBA, South Atlantic MOC Basin-wide Array.

reason, 34.5°S has been identified as a crucial latitude for examining the meridional transports of volume, heat, and salt due to the possibility that our current climate may be in a regime of multiple equilibria of the Atlantic Meridional Overturning Circulation (AMOC) and the need for observable transport metrics in the region (e.g., Dijkstra, 2007; Drifjhout et al., 2011; Huisman et al., 2010; Weijer et al., 2019). Observational and modeling results suggest that analysis of the boundary currents in the South Atlantic is essential to explore the local and remote forcing of AMOC fluctuations (e.g., Biastoch et al., 2008; Dong et al., 2009; Dong, Baringer, et al., 2011, Dong, Garzoli, et al., 2011; Rühs et al., 2015). While in the subtropical South Atlantic the warm upper limb of the AMOC primarily occurs at the eastern basin (e.g., Kersalé et al., 2019), the BC is unique as it carries mass and heat southward (i.e., in opposite direction of the AMOC) and recent studies have shown that changes in the BC transport contribute to low frequency variability that has been observed in South Atlantic meridional volume and heat transports (e.g., Dong et al., 2009; Dong et al., 2015). It is therefore essential to accurately quantify the BC transports and variability to close the meridional basin-wide volume and heat transport budgets in the South Atlantic (e.g., Garzoli & Matano, 2011). Furthermore, the BC variability has often been poorly resolved and/or reproduced by different models (e.g., Palma et al., 2004) and there are many open questions about the response of the BC to intensifying Southern Hemisphere westerly winds under global warming (e.g., de Souza et al., 2019; Drouin et al., 2021; Yang et al., 2020, 2016), highlighting the importance of observing and understanding the characteristics and long-term variability of the BC.

In recent years, observations of the BC have increased as the AMOC observing network has expanded into the South Atlantic (e.g., Ansorge et al., 2014; Frajka-Williams et al., 2019; Garzoli et al., 2012; Hummels et al., 2015; Meinen et al., 2013, 2018; Kersalé et al., 2020; Herrford et al., 2021). One element of this AMOC observing network, the South Atlantic MOC Basin-wide Array (SAMBA) has been under development at 34.5°S since 2009, and is presently being used to observe daily variations in the AMOC (Meinen et al., 2013, 2018; Kersalé et al., 2020). The western boundary component of SAMBA (termed "SAMBA-West") observes the flows of the BC in the upper ocean and the Deep Western Boundary Current (DWBC) below, and these observations provide the backbone of the present study between the continental shelf and 44.5°W (Figure 1; Table 1). The initial studies using the SAMBA-West array data have concentrated their analysis on the deep limb of the flow carried by the DWBC and the abyssal flows (Meinen

et al., 2012, 2017; Valla et al., 2019), and this is the first study focusing on the upper ocean currents on the western boundary.

The purpose of the present study is to examine the daily to interannual variability of the depth-integrated volume transport of the upper ocean, carried by the BC, by analyzing the SAMBA-West moored observations during a particularly well-observed segment of time between March 2009 and November 2015. These results will provide a better understanding of the strength, structure, and temporal variability of the upper branch of the WBCs in the South Atlantic by examining variations across a multitude of timescales with this unprecedented 6+ year data set.

2. Data and Methods

2.1. Overview of the SAMBA Array in the Western South Atlantic ("SAMBA-West")

This paper presents results from 6+ years of data from the SAMBA-West array between March 2009 and November 2015. The first component of the array was deployed in March 2009 and is still operating continuously (e.g., Kersalé et al., 2020; Meinen et al., 2012, 2017; Valla et al., 2018, 2019). The SAMBA-West array was designed to study the western boundary contributions to the AMOC, and it also represents the western cornerstone of the SAMBA array which measures the basin-wide integrated meridional volume and heat transport at 34.5°S (Kersalé et al., 2020; Meinen et al., 2013, 2018). The location of the array was chosen to be just north of the meander-window for the BMC, typically found around 38°S (e.g., Gordon & Greengrove, 1986; Goni et al., 1996, 2011; Lumpkin & Garzoli, 2011), to avoid the complicated variability of the confluence front and its energetic meanders (Meinen et al., 2012, 2017; Perez et al., 2011). Initially the array consisted of a line of three pressure-recording inverted echo sounders (PIES; Sites A, C and D) moorings and one current- and pressure-recording inverted echo sounder (CPIES; Site B) mooring deployed along 34.5°S spanning about 640 km between the 1360-m isobath at 51.5°W (Site A; Figure 1) and the 4757-m isobath at 44.5°W (Site D; Figure 1). The initial CPIES was later replaced with a PIES in 2011, and in December 2012 two additional CPIES moorings were deployed between the westernmost two pairs of the existing PIES moorings (Sites AA and BB) to improve the horizontal resolution of the array (e.g., Meinen et al., 2017). Furthermore, in December 2013 a bottom-mounted upward looking Acoustic Doppler Current Profiler (ADCP) mooring was deployed to capture meridional flows on the upper continental slope, nominally at the 411-m isobath (Figure 1, Table 1). Note that the first CPIES deployed at Site B functioned improperly in 2010 and was lost during a recovery attempt in 2011, and as a result there is a gap of about 2 months at the start of the first deployment at that site and of nearly 15 months in 2010–2011 at the end of that first deployment. The nominal positions, water depths and deployment dates of the PIES, CPIES, and ADCP moorings are given in Table 1 (see also Figure 1).

Table 1
Nominal Positions, Water Depths, and Initial Deployment Dates of the Instruments Distributed Across the SAMBA-West Transport Line at 34.5°S

Description	Site name	Longitude (west)	Latitude (south)	Water depth [m]	Date of first deployment
ADCP		51°40.0′	34°19.0′	411	December 14, 2013
PIES	A	51°30.0′	34°30.0′	1,360	March 18, 2009
CPIES	AA	50°31.2′	34°30.0′	2,885	December 11, 2012
PIES[a]	B	49°30.0′	34°30.0′	3,535	March 18, 2009
CPIES	BB	48°30.5′	34°30.0′	4,140	December 12, 2012
PIES	C	47°30.0′	34°30.0′	4,540	March 19, 2009
PIES	D	44°30.0′	34°30.0′	4,757	March 20, 2009

[a]The original CPIES deployed at Site B transmitted data poorly and/or incompletely during download cruises in August 2009, July 2010, and December 2010, so it was decided that it would be replaced with a new PIES during the next cruise in July 2011. The CPIES was lost during recovery, and as a result, there is a gap of about 2 months at the start of the deployment and nearly 15 months (March 21, 2010–July 10, 2011) at the end of the first deployment at that site.

Abbreviations: ADCP, Acoustic Doppler Current Profiler; CPIES, current- and pressure-recording inverted echo sounder; PIES, pressure-recording inverted echo sounder; SAMBA, South Atlantic MOC Basin-wide Array.

Table 2
Hydrography (CTD), Dissolved Oxygen (O_2), and LADCP Data Used in This Study

Cruise	Dates	Data type	Longitude range [west]
SAM02	August 17–25, 2009	CTD	51°29.0′; 44°28.0′
SAM03	July 5–16, 2010	CTD/O_2	51°29.0′; 44°27.0′
SAM04	December 20–29, 2010	CTD	51°29.0′; 44°27.0′
SAM05[a]	July 2–12, 2011	CTD/LADCP	51°40.0′; 44°31.0′
SAM07	July 2–12, 2012	CTD/O_2/LADCP	52°50.0′; 44°31.0′
SAM08	December 1–16, 2012	CTD/O_2	51°38.0′; 44°29.0′
SAM10[a]	October 4–16, 2014	CTD/LADCP	51°31.0′; 44°31.0′
STSF	October 7–8, 2013	CTD/LADCP	51°20.0′; 51°30.0′

Note. [a]LADCP section incomplete.

Abbreviations: CTD, conductivity, temperature, and depth; LADCP, Lowered Acoustic Doppler Current Profiler; SAMBA, South Atlantic MOC Basin-wide Array; STSF, SubTropical Shelf Front.

Between 2009 and 2015 seven cruises in support of SAMBA-West have been conducted roughly every 6 to 12 months (Table 2, labeled "SAM" followed by cruise number). During each cruise, conductivity, temperature, and depth (CTD) stations were occupied along the SAMBA-West line (white circles in Figure 1, Table 2). The SAMBA-West hydrographic sections, which are typically collected over 4–6 days, have a typical horizontal resolution of 20 km at the inner shelf and shelf-break and 45–90 km offshore. In addition to the basic CTD measurements, some of the cruises also collected quasi-continuous dissolved oxygen (O_2) profiles and lowered ADCP (LADCP) measurements of full-depth velocities (data processing is described in Valla et al., 2018, 2019). These hydrographic sections provide independent transport estimates as we will see in Section 3.2, which can be compared with the PIES/CPIES derived transports. Three of the SAMOC-West cruises also occupied additional stations inshore of the westernmost PIES (Site A) on the continental shelf and shelf-break, providing an essential mean transport estimate inshore of the westernmost moored PIES at Site A, as will be shown in Section 2.2.1. An additional shelf/upper slope CTD/LADCP section was taken in 2013 as part of the SubTropical Shelf Front (STSF) program (Berden et al., 2020; Charo, Guerrero, & Piola, 2020; Charo, Valla, et al., 2020). Data from the high-density XBT transect AX18, which nominally crosses the South Atlantic along 35°S between South America and South Africa quasi-quarterly since 2002 (e.g., Dong et al., 2009; Garzoli & Baringer, 2007; Garzoli et al., 2013), are also used to compare against the baroclinic geostrophic estimates from the PIES/CPIES array and the CTD sections. Processing for PIES/CPIES and ADCP measurements is explained in the following subsections.

2.1.1. PIES Data Processing and Gravest Empirical Mode

The IES has been in use as an oceanographic tool for about 50 years (e.g., Rossby, 1969; Watts & Rossby, 1977). In its basic form the IES measures the travel time τ for a sound pulse (originally 10 kHz, since the year 2000 generally 12 kHz) to travel from the sea bottom to the surface and back. The basic processing of the raw hourly IES τ measurements has been well established for many years and are described in detail elsewhere (e.g., Chidichimo et al., 2014; Donohue et al., 2010; Tracey et al., 1997). Early applications of the IES in the Southwestern Atlantic utilized hydrography-derived relationships between dynamic height anomaly integrated between the surface and a fixed pressure (often 300 dbar) and simulated travel time to estimate the baroclinic transport of the upper ocean currents relative to an assumed level of no motion (e.g., Garzoli & Bianchi, 1987; Garzoli, 1993). In the late 1980s and early 1990s, a variant instrument integrating a bottom pressure sensor was developed (PIES; e.g., Watts et al., 1995). The processing of the raw hourly bottom pressure data, which includes a "response analysis" tidal correction following Munk and Cartwright (1966), has been presented in detail elsewhere and will not be repeated here (e.g., Donohue et al., 2010; Watts & Kontoyiannis, 1990). Later in the early 2000s a version of the instrument adding a single-depth acoustic current meter 50 m above the bottom was also developed (CPIES; e.g., Bishop et al., 2012; Donohue et al., 2010; Greene et al., 2012). In essence the aforementioned papers illustrate how the hourly pressure and τ measurements are processed to produce a single daily value of τ and pressure at noon GMT each day. Subsequently, a 72-h low-pass filter is applied to the τ and pressure records at each site to remove tides.

Modern analysis of τ data involves the use of two-dimensional look-up tables that are created via the Gravest Empirical Mode (GEM) technique developed by Meinen and Watts (2000). The details of how τ data and bottom pressure measurements of a PIES (or CPIES) are combined with historical hydrography from the region via the use of the use of two-dimensional look-up tables that are created via the GEM technique to produce daily estimates of relative geostrophic velocity at the SAMBA-West array are presented in Meinen et al. (2012, 2013, 2017) and will not be repeated here. In brief, the GEM look–up tables quantify temperature (T), salinity (S), and/or specific volume anomaly (δ) as functions of pressure and τ calculated from

hydrographic casts between the surface and a selected reference pressure (1,000 dbar herein). The daily PIES-GEM estimated profiles are gridded with uniform 20 dbar pressure increments from the surface to the seafloor. The PIES-GEM δ profiles are then vertically integrated to give daily dynamic height anomaly (ϕ) profiles relative to an assumed level of no motion. Differencing the ϕ profiles at neighboring PIES/CPIES sites yields daily full water column profiles of the component of the relative geostrophic velocity perpendicular to the line between the sites (e.g., meridional) via the standard geostrophic method (e.g., Gill, 1982). Similarly, differencing the bottom pressure measurements at neighboring PIES/CPIES yields the temporal anomaly of the absolute geostrophic bottom velocity. However, the time mean absolute geostrophic bottom velocity cannot be determined due to the well-known leveling problem (Donohue et al., 2010; Meinen et al., 2012).

The products from a high-resolution numerical model are utilized to provide estimates of the time-mean bottom or reference velocities (the variability of the reference velocity comes from the bottom pressure observations). We use the time-average of 35 years of 3-day snapshots from the OGCM for the Earth Simulator (OFES) with 0.1° horizontal resolution and more than 50 vertical levels, provided by the Japan Agency for Marine-Earth Science and Technology (JAMSTEC) (e.g., Sasaki et al., 2008). Similar to previous studies in the region using data from the SAMBA-West array that have also selected this particular model run, the time-mean reference velocity was computed at 1,500 dbar (Meinen et al., 2013, 2017, 2018; Valla et al., 2019).

Herein, the time-mean meridional reference velocities used from the 35-year run from the OFES fields between 1980 and 2015 are −5.6, −6.0, 0.7, 0.7, and −0.2 cm s^{-1} between site pairs A-AA, AA-B, B-BB, BB-C, and C-D, respectively and −5.8 and 0.7 cm s^{-1} between site pairs A-B and B-C, respectively. Note, our results are not sensitive to using mean OFES 1500 dbar velocities for the same period as the observations (2009–2015) versus the 35-year mean that we used in this study.

Throughout this paper, we use the term "baroclinic" to refer to the transport estimated from geostrophic velocity shears referenced to zero at the bottom, and the term "barotropic" to refer to the transport contribution from the bottom-reference velocity (non-sheared term). The "absolute" transport is the sum of the baroclinic and the barotropic terms. Note that all of the time variability associated with the baroclinic and barotropic terms originate from the PIESs travel time τ and bottom pressure measurements, respectively, and hence are independent from the model time-mean reference velocities. The time-mean of the vertically sheared (baroclinic) term is also purely observational and independent from the model. The resulting time-mean transports are not hugely sensitive to the choice of the model to compute the time-mean meridional reference velocities (as shown in Meinen et al., 2017).

2.1.2. ADCP Data Processing

The data from the ADCP mooring deployed at 411 m depth on the upper continental slope in December 2013 (Figure 1, Table 1) were processed following standard procedures (e.g., Côté et al., 2011). The 150 kHz ADCP recorded hourly velocity on vertical bins of 16 m, with bins centered at depths between 23.73 and 343.73 m. The hourly data were averaged to obtain daily values, and subsequently a 72-h low-pass filter was applied to remove tides.

2.2. Absolute Brazil Current Transport Calculation

The calculation of a boundary current transport requires a choice of the vertical and zonal limits of integration. Along the SAMBA-West array, the neutral density surface (γ^n) of 27.1 kg m^3 separates the warm, salty, relatively low in oxygen Tropical Water (TW) and South Atlantic Central Water (SACW) from the relatively cold-fresh oxygen-rich Antarctic Intermediate Water (AAIW) located below (Valla et al., 2018; Figures 2a–2d). Thus to obtain the bulk of the BC transport, we calculate transports in the depth layers occupied by the TW and SACW by evaluating the γ^n structure (Jackett & McDougall, 1997) across the hydrographic sections (Figures 2a–2c; Table 2). We find the interface between SACW and AAIW on average at the 628 ± 46 dbar pressure level (variability represents one standard deviation; the shallowest and deepest positions observed during cruises are at 533 and 667 dbar, respectively), and we define this temporally fixed lower bound for integrating the velocities to obtain transport. The resulting transport time series are not significantly different for modest (±100 dbar) changes to the 628 dbar pressure level (correlation coefficient of 0.99 and root-mean-square error of 1.5 Sv). Note that at this latitude the western boundary flow is mostly southward over

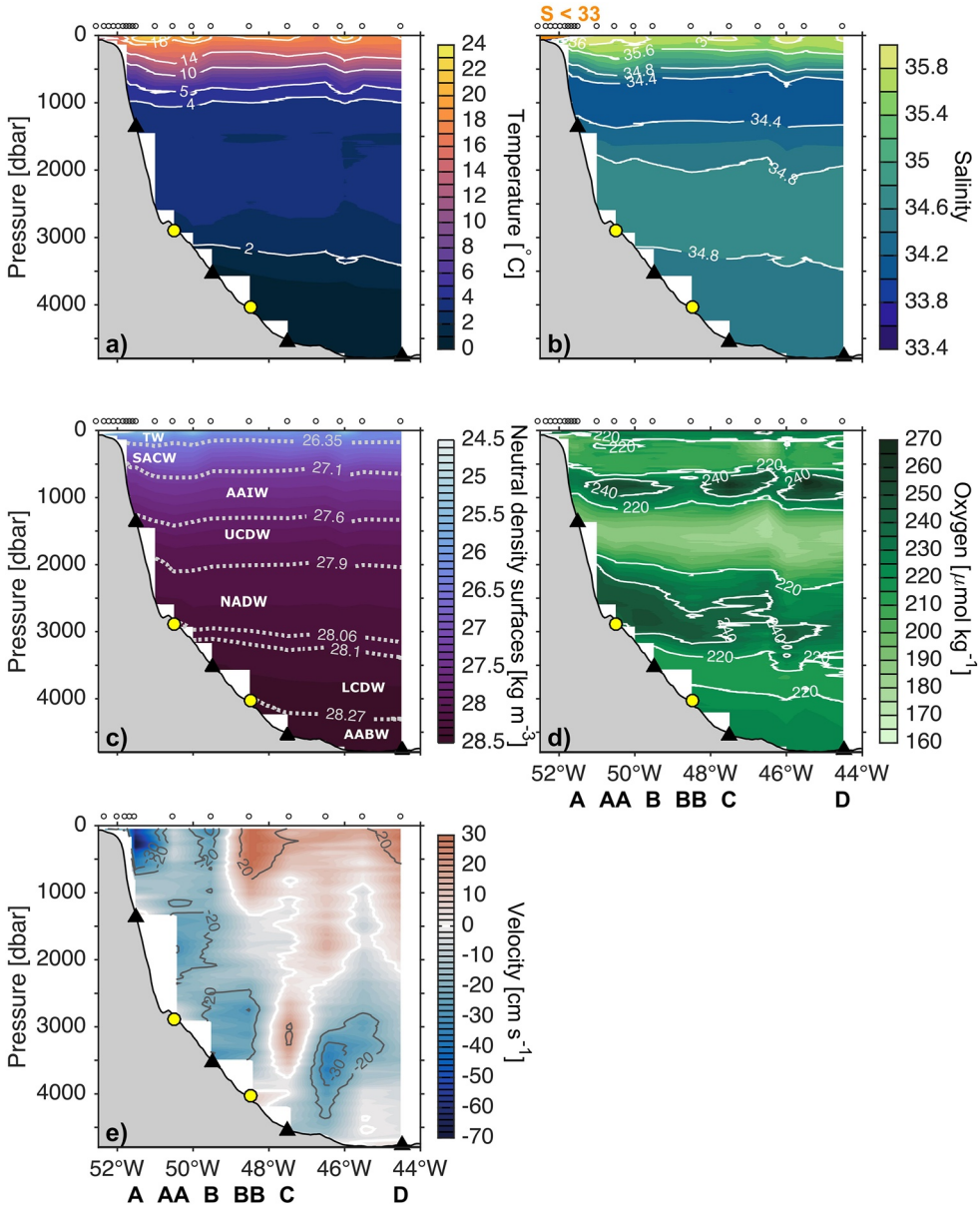

Figure 2. Average high-resolution hydrographic sections along the SAMBA-West line of (a) in situ temperature (°C), (b) salinity, and (c) neutral density surfaces (γ^n; kg m^{-3}) during four hydrographic cruises (SAM05, SAM07, SAM08, and SAM10; Table 2), (d) dissolved oxygen (μmol kg^{-1}) during SAM07 and SAM08, and (e) alongshore velocity (cm s^{-1}) derived from LADCP velocities collected during SAM07 cruise during July 2012 (white contours indicate zero flow; negative velocities, blue shading, indicate southward flow). A 50 m moving average is applied in the vertical to the alongshore velocity profiles for stations deeper than 400 m in order to reduce noise in the LADCP data. Acronyms in panel (c) indicate the key water masses after Valla et al. (2018): TW: Tropical Water; SACW: South Atlantic Central Water; AAIW: Antarctic Intermediate Water; UCDW: Upper Circumpolar Deep Water; NADW: North Atlantic Deep Water; LCDW: Lower Circumpolar Deep Water; AABW: Antarctic Bottom Water. White circles on top of the upper axis represent the nominal positions of the hydrographic CTD/O_2 stations (identical to Figure 1) in panels ((a), (b), (c), (d)) and the positions of the hydrographic LADCP stations during SAM07 in panel (e). Gray shading is the bathymetry from the Smith and Sandwell (1997) data set. PIES and CPIES locations are indicated by the black triangles and yellow circles, respectively, on top of bathymetry of each panel. Labels at the bottom of panels (d) and (e) indicate the names of the PIES/CPIES sites. CPIES, current- and pressure-recording inverted echo sounder; CTD, conductivity, temperature, and depth; LADCP, Lowered Acoustic Doppler Current Profiler; PIES, pressure-recording inverted echo sounder; SAMBA, South Atlantic MOC Basin-wide Array.

the entire water column so it is not possible to establish more quantitative, time-varying, criteria to separate the BC from the DWBC, such as a zero-velocity crossing. For similar reasons, Meinen et al. (2017) chose 800 dbar as the upper bound to obtain the DWBC flow.

The definition of the horizontal limits of integration to estimate transports from in situ arrays is also not straightforward, as they strongly depend on the array's spatial resolution as well as on eddies/meanders passing by the array's laterally separated sites at each time step. Defining a static box within which a "total" (or "absolute") BC transport will be calculated will certainly include transient transports from Rossby Waves and other features, which propagate into the integration domain. Even utilizing time-varying integration boundaries based on characteristics of the ocean flow, such as stream-coordinates, will still incorporate these other features when they superimpose on top of the main current (e.g., Meinen & Luther, 2016). As a result, the measured southward "Brazil Current" transport will fluctuate higher or lower, potentially reaching zero or even flowing northwards due to the influence of large eddies and other features (e.g., Meinen et al., 2017). For this study, the BC transport will be calculated within fixed boundaries determined from the available LADCP ship section (Figure 2e and Table 2), which as we will see later agree well with the PIES/CPIES time-mean velocity section.

The full-depth spatial structure of alongshore flow from the LADCP section (Figure 2e) evidences southward flow between the shelf break and Site B (at 49.5°W) from the surface to the bottom, with the BC core at the ~100–400 dbar range near the continental slope. Offshore of Site B there is a northward recirculation. Thus, an integration domain between the coastline and Site B, and between the surface and 628 dbar (i.e., the $\gamma^n = 27.1$ kg m^3 surface) is selected. We will come back to the analysis of the horizontal extent of the BC in the following sections. The "absolute" BC transport represents the sum of the baroclinic and barotropic velocities integrated over this domain.

Note, we find that the wind-forced Ekman transport contribution to the BC in this region is very weak, and it has a very small temporal mean and standard deviation of -0.002 ± 0.225 Sv during 2009–2015 (not shown). Additionally, the SAMBA-West array location is close to the zero value of the wind stress curl (e.g., Schmid & Majumder, 2018). Thus, we focus on the geostrophic component of the BC transport in this study.

To obtain the total flow above 628 dbar associated with the BC, we compute transports through two cross-sectional areas and afterward sum them: (i) over the upper continental slope inshore of the 1,360 m isobath between the coast and Site A (Section 2.2.1); and (ii) between Site A (1,360 m isobath) and Site B (3,535 m isobath) (Section 2.2.2).

Note that the full details on the estimation of the total transport accuracy are provided in Appendix A. Throughout this paper and unless otherwise noted the reported velocity/transport/pressure variability represents one standard deviation from the time-mean and negative velocities/transports indicate southward flow.

2.2.1. Transport on the Shelf and Upper Continental Slope

Due to the more limited data inshore of Site A, several different approaches were applied to estimate the transport within that wedge. A preliminary first estimate of the time-mean flow inshore of Site A was determined by evaluating the alongshore transport from the three snapshot hydrographic sections that included absolute velocity measurements with an LADCP between the 400 m isobath and Site A. Integrating the LADCP profiles from three cruises over a distance of 29 km between the 400-m isobath and Site A (1,360 m isobath) and from the surface to 622 m depth gives a mean and standard deviation of the transport of -2.4 ± 0.8 Sv. A second estimate of -2.7 ± 1.5 Sv was determined using all CTD data available (-3.0 ± 1.8 Sv for the three cruises that also collected LADCP observations) to estimate the velocity shear between the surface and the $\gamma^n = 27.1$ kg m^3 surface relative to the deepest common level (i.e., the bottom) between stations from each of the cruises that sampled between the 400 m isobath and Site A (Table 2; Figure 3b). This estimate is in good agreement with the LADCP mean estimate. The vertical structure of the CTD and the spatially averaged LADCP shear profiles between station pairs also agree fairly well for three cruises with both types of data (see for example light green dotted and solid lines in Figure 3b).

Analyses of the velocity data collected with the moored ADCP at the 411-m isobath, only available between December 2013 and November 2015, provides further insights about the shelf and upper slope velocities.

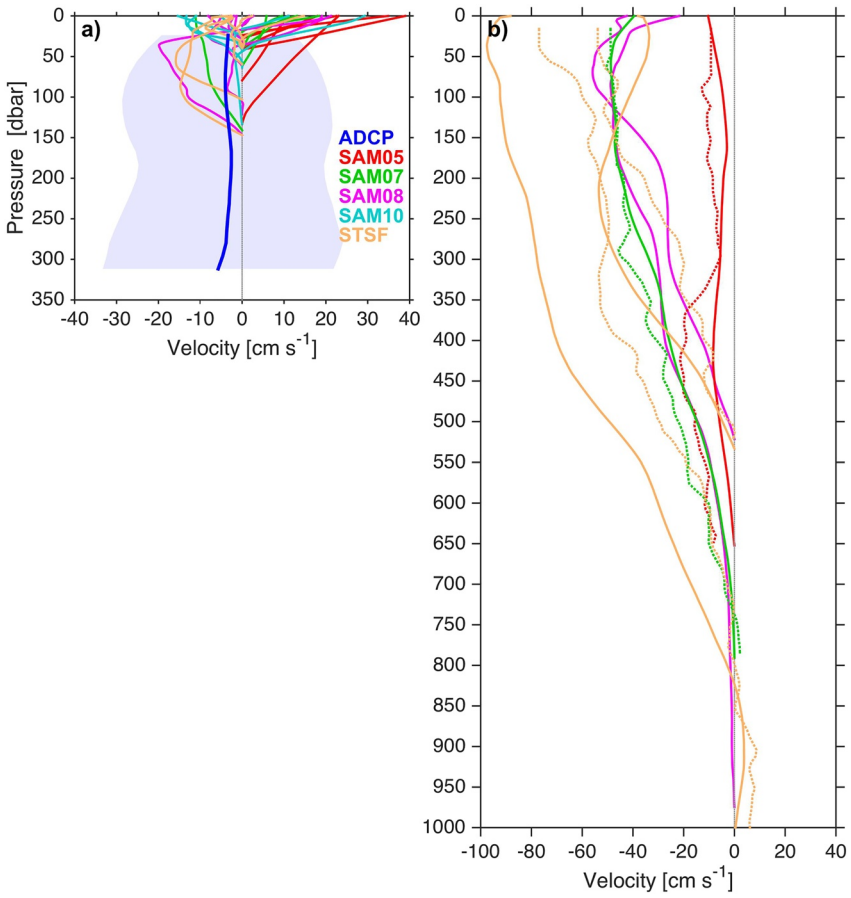

Figure 3. Alongshore velocity on the shelf and continental slope inshore of Site A. (a) Time-mean velocity profile from the moored ADCP (blue line) and standard deviation (blue shading) are shown as well as the geostrophic velocity profiles from CTD station pairs (solid red, light green, magenta, light blue, and orange lines) for stations shallower than 400 m from the cruises indicated in the legend. Note the absolute velocity profiles from LADCP in this region are not shown for clarity. (b) Geostrophic velocity profiles from CTD station pairs (solid red, light green, magenta, and orange lines) and spatially averaged absolute velocity profiles from LADCP between station pairs when available (dotted red, light green, and orange lines) for sites between the 500 m isobath and Site A (at 1,360 m) from the cruises indicated in the legend in (a). No CTD/LADCP profiles are available in this region during SAM10. Negative velocities indicate southward flow. Note, the different velocity scale on the *x*-axes for (a) and (b). CTD, conductivity, temperature, and depth; LADCP, Lowered Acoustic Doppler Current Profiler; SAMBA, South Atlantic MOC Basin-wide Array.

The time-mean flows from the ADCP (Figure 3a, blue line) are weak compared to the snapshot CTD relative velocities and the LADCP absolute velocities that are found for the stations at the 500–1,000 m isobath range (Figure 3b). The standard deviations of the moored ADCP velocities are quite large (Figure 3a, blue shading), however, which suggest large meridional velocity variability at this location consistent with the large spread of velocities observed during each cruise (shallow profiles on top of blue profile, Figure 3a). The mean moored ADCP velocities instead agree well in magnitude with the CTD relative velocities (solid red, light green, magenta, light blue, and orange lines) and LADCP velocities (not shown) up on the shelf for depths shallower than 200 m, which are very likely unrelated to the BC. We note that high-resolution numerical models have previously estimated weak seasonal reversing flows of ~−0.4 to 0.3 Sv on the continental shelf inshore the 500 m isobath near 32°S (Palma et al., 2008).

The relatively small transports in the western wedge that are not sampled by the PIES/CPIES array (−2.4 Sv from LADCP; −2.7 Sv from CTD) agree fairly well with previously published estimates based on long-runs of the OFES model (−3.0 ± 1.6 Sv) and the Nucleus for European Modeling of the Ocean (NEMO) model (−4.6 ± 3.3 Sv) as well as from 18 XBT sections (−2.1 ± 2.5 Sv) in Meinen et al. (2013). The limited cruise snapshot data together with the moored ADCP data suggest that the largest portion of the flow not presently

sampled by the PIES/CPIES array is concentrated within the ~25 km immediately west of Site A between the 500 and 1,000 m isobaths (Figure 3b), with large southward velocities reaching up to nearly −100 to −40 cm s^{-1} in the upper 400 m of the water column during individual cruises. Figure 3b also demonstrates that the vertical structure of the velocity profiles inshore of Site A has a very "baroclinic" structure which clearly varies over time. Although a small number of snapshots are not representative of the multi-year long-term mean wedge transport, the best available option for estimating the transport within this inshore wedge is to use the average of the cruise section data. Because there are more CTD sections than LADCP sections, we have elected to use the mean CTD estimate (−2.7 Sv) on the shelf-break.

2.2.2. Transport From PIES/CPIES

The transport within the PIES/CPIES array was integrated between pairs of moorings following well-established methods (e.g., Meinen et al., 2017, and references therein; Section 2.1.1). Based on the meridional velocity section in Figure 2e the southward flow of the BC Current is concentrated west of 49.5°W. Sites A (at 51.5°W) and B (at 49.5°W) constitute the primary endpoints for this calculation because the records at those two sites span the longest time period (2009–2015).

Recall that in December 2012 two CPIES were deployed midway between Sites A and B (Site AA) and between Sites B and C (Site BB) (Figure 1, Table 1). Geostrophic flow is naturally integrating, so including an additional site between two neighboring sites does not change the geostrophic flow integrated between the two original sites. In practice, however, transports determined using the central site or excluding the central site will not be identical in the presence of sloping bottom topography. Furthermore, the use of additional sites can reduce the size of unobserved bottom triangles along that slope. In order to test the impact of the increased horizontal resolution between Sites A and B during 2013–2015, we estimate transports between Sites A and B during those 3 years including Site AA. There is no significant change in the mean transport and its variability compared with the estimate excluding AA (correlation coefficient of 0.98 and root-mean-square error of 1.0 Sv) indicating that the velocity in the unobserved bottom triangles when using only Sites A and B for the calculation are very small. To test the transport contributions between Sites B and BB, we evaluate the transport from B to BB for each time step; interestingly the time-mean absolute transport between these two sites was positive (northward) during 2013–2015 (4.9 ± 7.6 Sv), which decreases the BC southward transport if included. The resulting time-mean absolute transport between Site B and Site BB in the BC depth layer when only the periods of southward flow in that span are averaged (with the condition that transports between Sites A and B are also southward) is only −1.0 ± 1.6 Sv, and would increase the southward BC transport only very slightly if included. Because Site BB is not always available during 2009–2015, we decided to only use Sites A and B as endpoints for our calculation recognizing that we may occasionally miss a minimal fraction of the BC transport offshore of Site B.

We determine the absolute BC transport as follows. First, we add a constant (time-mean) slope transport of −2.7 Sv from the average of the CTD sections (Section 2.2.1) to the time-varying baroclinic PIES transport time series referenced to zero at the bottom (Section 2.1.1), hereafter referred to as the baroclinic component of the BC transport. Next, we estimate the barotropic BC transport component as described in Section 2.1.1. Finally, we combine the baroclinic and barotropic components to obtain the absolute BC transport. The resulting transport time series will be presented and discussed in the following section.

3. Results and Discussion

3.1. Brazil Current Absolute Velocity and Transport Variability

The spatial structure of the time-mean absolute velocity section from the PIES/CPIES data shows southward flow from the surface to the ocean bottom between Sites A and B (Figure 4a) with peak southward speeds reaching −12 cm s^{-1} near the surface. This southward flow includes both the BC above ~628 m (based on the density interface definition), and the DWBC below the BC base; as in previous studies with the SAMBA-West array, there is no obvious indication in the time-mean velocity field as to where one current ends and the other current begins (Meinen et al., 2012, 2017). The BC is concentrated west of 49.5°W (Figures 4a, 4c, and 4e) in agreement with the hydrographic section (Figure 2e). When CPIES records at AA and BB are included, the peak speeds within the BC core are faster (compare Figures 4c and 4e) by approximately 4 cm s^{-1} between Sites A and AA, due to less horizontal averaging, but the integrated transports

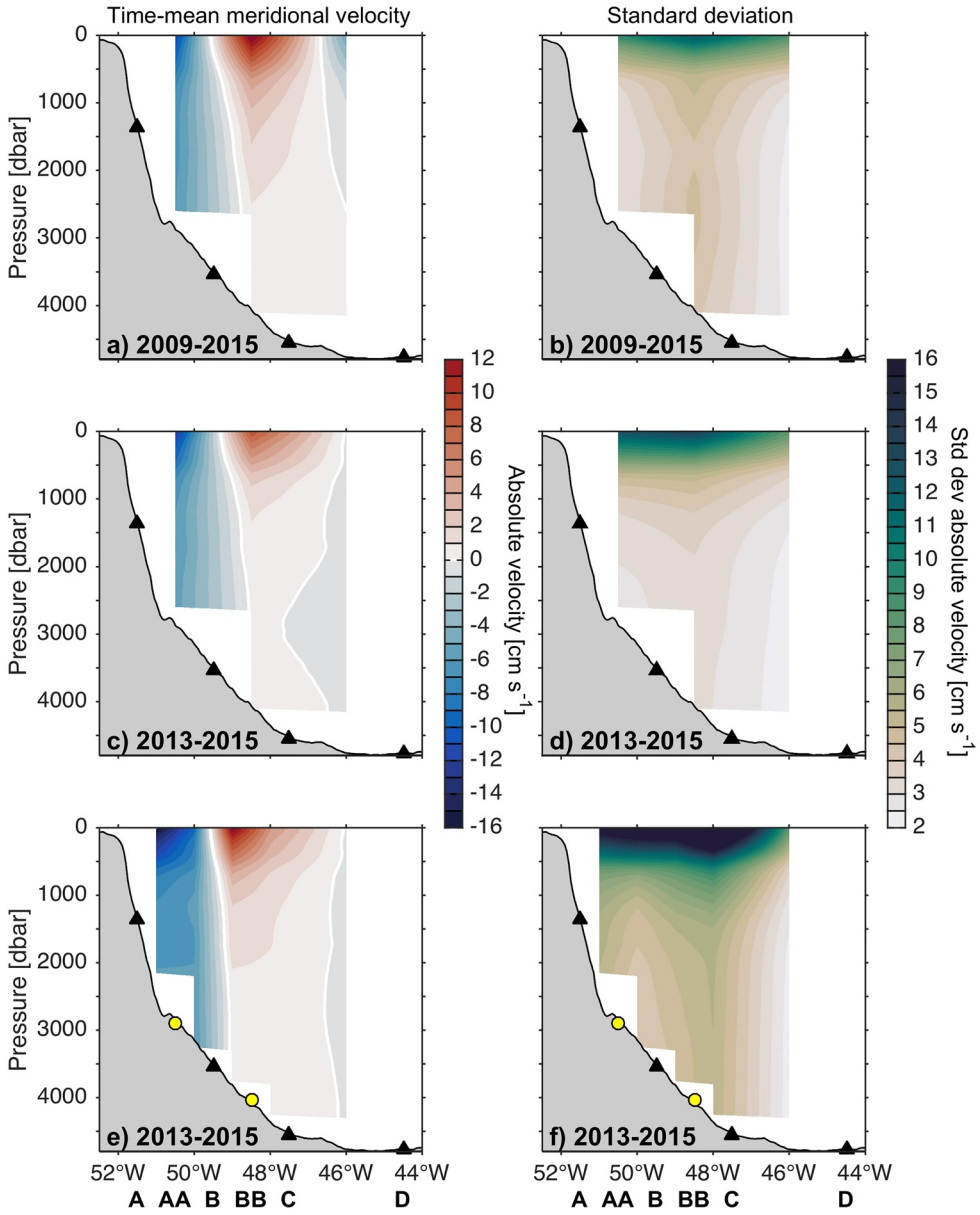

Figure 4. Time-mean absolute meridional velocity between PIES/CPIES station pairs along the SAMBA-West array (left panels) and temporal standard deviation (std dev) of the absolute meridional velocity (right panels). The time-mean and temporal standard deviation of the absolute meridional velocity are computed for (a), (b) the full period of PIES measurements (2009–2015), (c), (d) for the period when the horizontal resolution of the array was augmented with CPIES AA and BB but only using the PIES data (2013–2015), and (e), (f) for the period when the horizontal resolution of the array was augmented with CPIES AA and BB using all available data (at Sites A, AA, B, BB, C and D) (2013–2015). White contours in left panels indicate zero flow. Negative velocity indicates southward flow. Labels at the bottom of panels (e) and (f) indicate the names of the PIES/CPIES sites. CPIES, current- and pressure-recording inverted echo sounder; PIES, pressure-recording inverted echo sounder.

are very similar as is to be expected in a geostrophic calculation when velocity at the unresolved bottom triangles is small (Section 2.2.2). Offshore of Site B (at 49.5°W) an evident northward recirculation can be observed in the full water column extending to 46°W, and further east of Site C the flow becomes southward again (Figures 4a, 4c, and 4e) as also observed by Meinen et al. (2017) for the period 2009–2014. The temporal standard deviation of the absolute velocity profiles (Figures 4b, 4d, and 4f) display large variability across the array from the surface to the bottom, with the largest variability between the surface and about

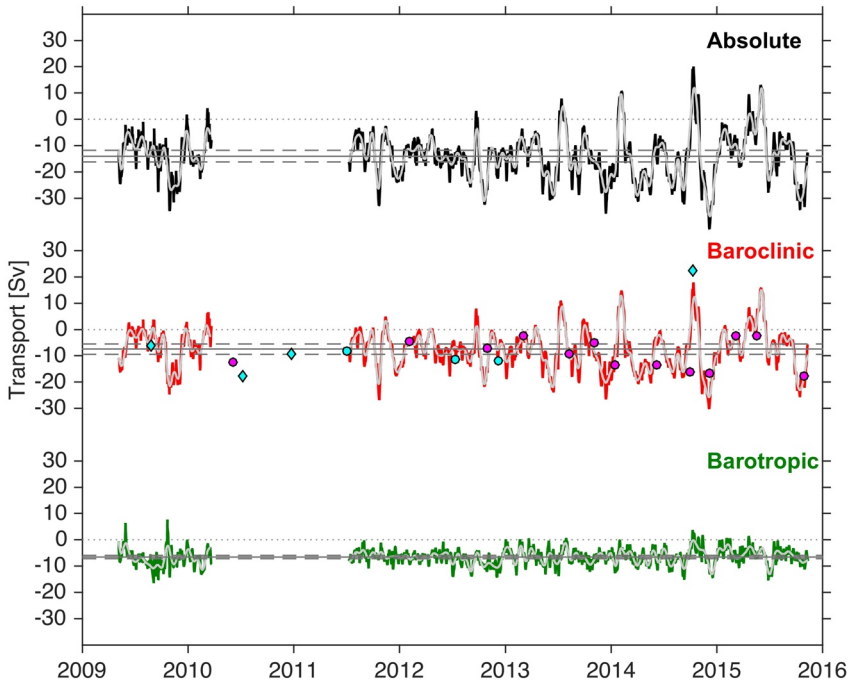

Figure 5. Time series of 72-h low-pass-filtered absolute (black), baroclinic (red), and barotropic (green) Brazil Current transport observed at 34.5°S during 2009–2015. The thin gray lines overlaid on top of each time series are the 30-day low-pass-filtered records. The gray horizontal solid and dashed lines indicate the time-mean and time-mean plus minus two standard errors of the mean (2*SEM; 95% confidence value), respectively. The cyan symbols indicate baroclinic transports estimated from concurrent hydrographic transects during the SAMBA-West cruises (circles and diamonds represent cruises with and without data inshore Site A, respectively; Table 2), and the magenta circles indicate the baroclinic transports computed using the measurements at the AX18 XBT line nominally at 35°S. Negative transports correspond to southward flow. SAMBA, South Atlantic MOC Basin-wide Array.

1,000 dbar. When including AA and BB in the calculation, the temporal standard deviation reaches nearly 16 cm s^{-1} at the BC core (comparable to the northward recirculation region) (Figure 4f). While the standard deviation provides evidence of strong surface intensification, the subsurface variability of the BC is also substantial (e.g., Figure 4b) and it is further enhanced with the addition of data from two more moorings (Figure 4f).

The absolute, baroclinic, and barotropic BC transport records during 2009–2015 exhibit means and standard deviations of −14.0 ± 8.8 Sv, −7.4 ± 7.6 Sv, and −6.6 ± 3.1 Sv, respectively (Figure 5; Table 3). The Standard Error of the Mean (SEM) of the absolute transport is 1.1 Sv based on the estimated 64 degrees of freedom in the record (Appendix A). The three time series all have large temporal variability with respect to their time-mean value, consistent with what has been observed in the DWBC below/offshore of the BC (Meinen et al., 2017). There are several times when the absolute transport (black curve in Figure 5) is positive (northward) or close to zero, for example, for the periods centered on March 9, 2010, September 21, 2012, February 5, 2014, October 12, 2014, and May 31, 2015. These periods of positive (or close to zero) absolute transport are mainly due to changes in sign of the baroclinic velocity component (compare black and red curves in Figure 5). The absolute transport time series exhibits a peak-to-peak transport range of 61.7 Sv, with maximum southward flow of −41.7 Sv on December 6, 2014, and maximum northward flow of 20 Sv on October 12, 2014. There is large short-term variability in the record, with changes of up to 20–30 Sv occurring over periods as short as 2–3 weeks, for instance between November 24 and December 11, 2009, September 2 and September 22, 2012, June 15 and July 9, 2013, January 20 and February 4, 2014, and September 17 and October 7, 2014 (black curve in Figure 5). Transport variations from peak-to-peak of ~40–45 Sv are observed over periods of 30–60 days, for example, between December 13, 2013 and February 4, 2014, and September 7 and October 12, 2014, and even larger peak-to-peak changes of ~50–60 Sv are observed between mid-October 2014 and early December 2014.

Table 3
Basic Statistics of the 72-h Low-Pass Filtered Absolute, Baroclinic, and Barotropic Brazil Current Transport Between 2009 and 2015

	Mean ± standard deviation [Sv]							
	2009	2010	2011	2012	2013	2014	2015	Average 2009–2015
Absolute	−14.0 ± 7.4	(−12.1 ± 6.0)	(−12.8 ± 6.9)	−14.7 ± 5.7	−14.8 ± 8.0	−16.2 ± 12.0	−10.8 ± 9.8	−14.0 ± 8.8
Baroclinic	−7.0 ± 7.0	(−4.7 ± 4.5)	(−6.9 ± 6.7)	−7.4 ± 4.8	−8.5 ± 7.4	−9.5 ± 9.7	−5.1 ± 8.2	−7.4 ± 7.6
Barotropic	−7.0 ± 3.7	(−7.4 ± 3.0)	(−5.9 ± 2.1)	−7.3 ± 2.5	−6.3 ± 2.7	−6.7 ± 3.5	−5.7 ± 3.0	−6.6 ± 3.1

	Median [Sv]	Min [Sv]	Max [Sv]	ITS [days]/DOF	SEM [Sv]
Absolute	−13.6	−41.7	20.0	12/64	1.1
Baroclinic	−7.0	−30.2	17.8	12/64	1.0
Barotropic	−6.5	−16.5	7.7	63/125	0.3

Note. (top) The mean and standard deviation of annual and average transports are given in columns 2–9. The mean annual values for years with less than eight months are given in brackets (years 2010 and 2011 have three and six months of available data, respectively). (bottom) The median, minimum and maximum values are given in columns 2–4. The integral time scale (ITS, days) and the degrees of freedom (DOF) are given in column 5 and the standard error of the mean (SEM) is given in column 6 (see Appendix A).

Abbreviations: DOF, degrees of freedom; ITS, integral time scale; SEM, Standard Error of the Mean.

The baroclinic transport also exhibits a large peak-to-peak transport range of 50 Sv, with similar rapid changes observed over short periods (red curve in Figure 5). The barotropic transport peak-to-peak range of 24.2 Sv is smaller than for the baroclinic record but it is still quite large. The barotropic transport also has fast changes of approximately 15–20 Sv during short periods of time, for instance between December 12, 2012 and January 2, 2013, and September 12, 2014 and October 7, 2014 (green curve in Figure 5). As with the peak-to-peak ranges, the standard deviation of the barotropic transport is smaller than that of the baroclinic transport (3.1 vs. 7.6 Sv, respectively). The large amplitude fluctuations in the three records persist even after 30-day low-pass-filtering the records using a sixth order Butterworth filter applied forward and backward to avoid phase shifts (Emery & Thomson, 2001; gray curves superimposed on black, red and green curves, Figure 5).

The correlation coefficient (r) between the baroclinic and absolute transport is high ($r = 0.92$; significant with 99% confidence, Appendix A). In contrast, the correlation between the baroclinic and barotropic components of the transport is quite low ($r = 0.31$) but significant with 95% confidence, and increases only slightly after applying a 30-day low-pass filter to both records to remove the high frequency signals ($r = 0.42$; significant with 95% confidence). The coherence spectra between the two records indicates that the time series are moderately correlated ($0.40 < r < 0.50$) for a narrow coherence period band centered at about 100 days, but are poorly coherent at other periods (not shown). The variability of the baroclinic component accounts for the largest fraction of the absolute transport variability (85%), confirming that the BC is mostly driven by changes in the baroclinic density field, but also indicating that the variability of the barotropic component is significant, accounting for 15% of the variance of the absolute transport.

3.2. Comparison With Other Transport Estimates

Historical BC transport studies have used different methods to define the depth of the base of the current and to determine its zonal extent, and most of these studies have not accounted for the barotropic component of the flow. Therefore, comparison among the different estimates is not straightforward. Furthermore, the BC has considerable transport variations along its southward path (e.g., Goni et al., 2011; Olson et al., 1988), with baroclinic values ranging from −1.5 Sv to −4.9 Sv to −13.2 Sv at 22°, 24°, and 34.5°S, respectively, all calculated using data collected during the same A09 cruise in 2009 (Bryden et al., 2011; King & Hamersley, 2010). As such, the most useful comparison is with other measurements collected close to our mooring locations at 34.5°S. Near 37.5°–38°S, a time-mean baroclinic transport of −10 Sv relative to and above 800 m was reported by Garzoli and Bianchi (1987) from 8 months of data from two IES moorings. This value yields roughly one third larger southward flow than our time-mean baroclinic estimate of −7.4 Sv, but the difference is well within our standard deviation of 7.6 Sv. During the Confluence Program

study in 1988–1990 (Garzoli, 1993), a much larger southward baroclinic transport was found, −24 Sv at 35.2° and 36.5°S. Because these historical observations were collected a decade or more before our new results, it is difficult to know whether the observed differences are due to temporal variability between the two time periods or are the result of observational/methodological differences.

The highly spatially resolved hydrographic sections taken along 34.5°S during the SAMBA-West cruises (Table 2), yield a mean and standard deviation of the transport of −6.6 ± 13.0 Sv (cyan circles and diamonds in Figure 5), which agrees well with the PIES baroclinic transport time series mean and standard deviation of −7.4 ± 7.6 Sv (red curve in Figure 4, Table 3). Note that these hydrographic CTD T and S profiles measured during the SAMBA-West cruises were not included in our GEM construction, thus allowing an independent comparison between the PIES/CPIES-derived estimates and the baroclinic transport estimates from hydrography. The even higher spatially resolved XBT NOAA transect AX18 along 35°S (e.g., Dong et al., 2015; Garzoli & Baringer, 2007; Garzoli et al., 2013), which has been maintained since 2002, gives a mean and standard deviation for the baroclinic transport relative to and above 800 m between 2010 and 2015 of −9.5 ± 5.8 Sv (the XBT transect was not occupied in 2009). Most of these XBT transects were occupied on average during periods of relatively enhanced southward flow (magenta circles in Figure 5), which explains the slightly enhanced southward baroclinic transport and highlights again the need for continuous measurements to avoid aliasing.

Historical estimates of the absolute transport, including both baroclinic and barotropic components of the flow, are fewer in number and have included a combination of XBTs, Argo, models, and satellite altimetry. Goni and Wainer (2001) found −14.0 ± 7.0 Sv from a TOPEX/POSEIDON ground track crossing the BC near 35°S, in good agreement with our measurements. At 35°S, a combination of *in situ* data from the AX18 XBT line and a model-based barotropic adjustment yielded an absolute transport of −19.4 ± 4.3 Sv (Garzoli & Baringer, 2007; Garzoli et al., 2013). More recently, meridional transports of the BC at 35°S in the upper 800 m were estimated as −12.6 ± 2.6 Sv at 34.5°S using Argo and altimetry data (Schmid & Majumder, 2018). While the temporal mean values from the XBT/model adjusted and Argo/altimetry products (−19.4 and −12.6 Sv, respectively) are relatively close to the value we find with the SAMBA-West data (−14.0 Sv), their transport standard deviations (4.3 and 2.6 Sv, respectively) are considerably smaller than what is found with the daily (8.8 Sv) or even with the 30-day low-pass filtered (8.2 Sv) SAMBA-West data. This is almost certainly due to the lower sampling rates of the XBT/model adjusted (quasi-quarterly transects) and Argo/altimetry (7–10 days repeats for altimetry & Argo) products. The lower sampling rates will miss the high frequency variability and rapid changes in the transport that are captured by the SAMBA-West data (Section 3.1; Figures 5 and 6). An additional disadvantage of the Argo-based product is that Argo data are not available on the continental shelf and upper slope, as floats are generally not deployed inshore of the 2,000 dbar isobath to reduce the chances of float grounding (e.g., Riser et al., 2016). Thus Argo-based estimates will miss the portion of the BC inshore of the 2,000 dbar isobath which as we have shown is a significant portion of the current (e.g., Figures 2e, 3b and 4e).

Our absolute time-mean transport estimate from SAMBA-West is not particularly sensitive to the choice of the reference level to compute the time-mean meridional reference absolute velocities from the high-resolution OFES run (Section 2.1.1). Choosing different reference levels instead of 1,500 dbar yields differences of −0.6 Sv (stronger southward flow) and 1.7 Sv (weaker southward flow) in the resulting time-mean absolute transport when choosing 1,200 or 2,100 dbar, respectively. Similarly, if the time-mean reference velocity at 1,500 dbar was 10% larger or 10% smaller the resulting transport estimates would differ by only −0.7 Sv (stronger southward flow) or 0.6 Sv (weaker southward flow). Recall the OFES model is only used to provide the time-mean reference velocity value of the non-sheared (barotropic) term, the variability of the barotropic component is purely observational as is the time-mean and temporal variability of the sheared (baroclinic) term (Section 2.1.1).

3.3. Spectral Distribution of Energy of the Observed Brazil Current Transport

Band-pass filtering the time series into bands with periods shorter than 30 days, periods between 30 and 150 days, and periods longer than 150 days shows that nearly 70% of the absolute transport variance is associated with periods between 30 and 150 days, while periods longer than 150 days account for only 19% of the variance, demonstrating a large variability on monthly and shorter time scales (Table 4). Similarly, 70%

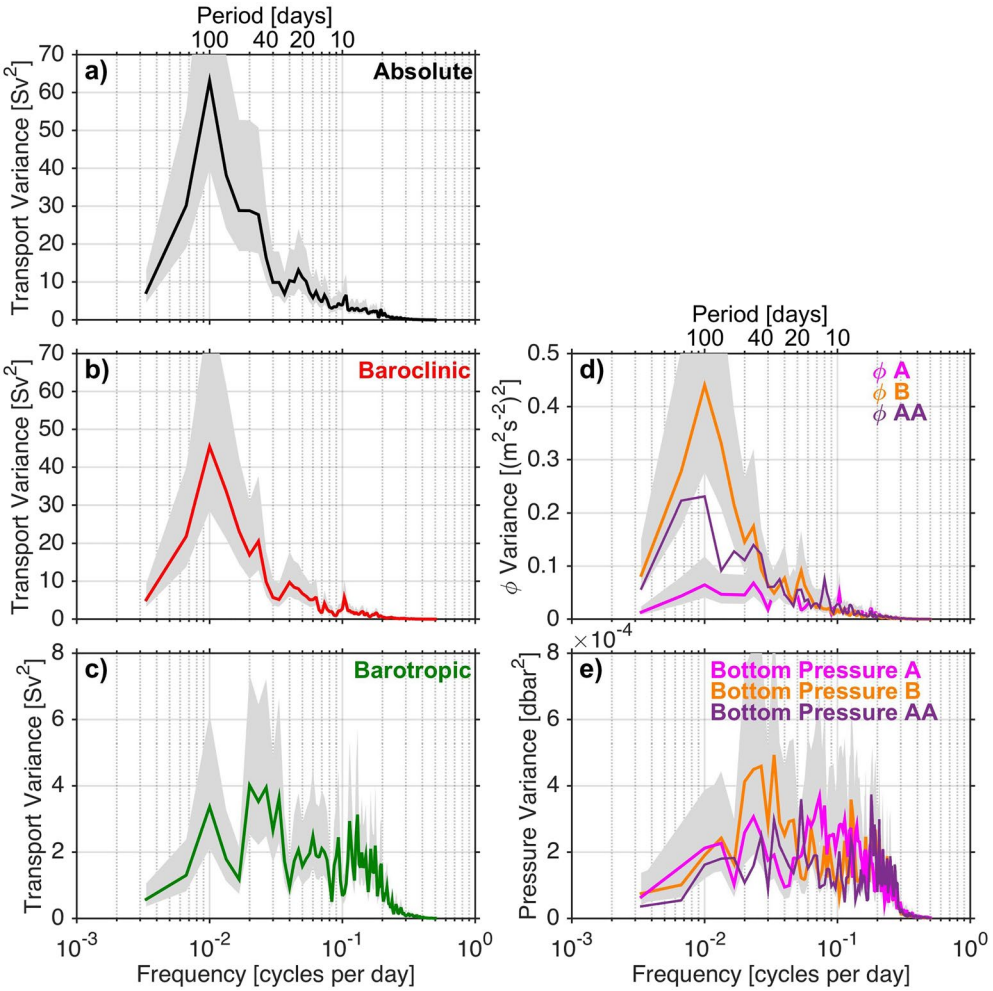

Figure 6. Variance preserving spectra of daily 72-h low-pass filtered (a) absolute, (b) baroclinic, and (c) barotropic Brazil Current transport time series. Note the different scale on the *y*-axes for (c). The variance preserving spectra of ϕ relative to the bottom integrated in the upper layer between the surface and the interface between TW/SACW and AAIW (on average at about 628 dbar) at Site A (magenta) and Site B (orange) are shown in (d) and the variance preserving spectra of bottom pressure at site A (magenta) and site B (orange) are shown in (e). Shaded confidence interval (95%) is also shown. The spectra of dynamic height (ϕ) and bottom pressure at Site AA (at 50.5°W midway between Sites A and B) for the period 2013–2015 are also shown in panels (d) and (c) respectively (purple lines; shaded confidence interval is not shown for clarity) to allow comparison. Recall that the time series at Sites A and B constitute the endpoints for the transport calculations. The spectra are computed based on Welch's periodogram method using 300-day-wide Hamming window and 150-day of overlap between consecutive data segments. AAIW, Antarctic Intermediate Water; SACW, South Atlantic Central Water; TW, Tropical Water.

of the baroclinic transport variance is associated with periods between 30 and 150 days, while for the barotropic transport a much larger fraction of the variance (40%) is associated with periods shorter than 30 days compared with what is found for the baroclinic term (11%) (Table 4).

In order to evaluate more precisely how the energy in these records is distributed by time scale, the spectral frequency distributions of the transport time series were computed using the longest portion of the records with continuous measurements (2011–2015) via Welch's periodogram method using a 300-day-wide Hamming window allowing 150 days of overlap (Emery & Thomson, 2001; Welch, 1967). The spectrum of the absolute transport (Figure 6a) has a significant broad peak centered at 100 days and a much less prominent and noisier peak near 20 days. The spectrum of the baroclinic transport also has significant energy near 100 days and a secondary and noisier peak near 20 days (Figure 6b). The barotropic transport spectrum is noisier (Figure 6c) with several shorter period peaks (less than 150 days), with the most prominent peaks at

Table 4
Variance (Sv^2) and % of Variance Explained for Different Period Bands in the Observed Absolute, Baroclinic, and Barotropic Brazil Current Transports

	Variance explained (Sv^2) (percentage)		
	3–30 days	30–150 days	More than 150 days
Absolute	9.2 (12%)	53 (69%)	15 (19%)
Baroclinic	6 (11%)	39 (70%)	11 (19%)
Barotropic	4 (40%)	5 (50%)	1 (10%)

Note. The statistics correspond to the period of continuous measurements between July 2011 and November 2015 (same period used to compute the spectra in Figure 6).

40–50 and 100 days. The large high-frequency content in all of these records highlights again the importance of continuous measurements with high temporal resolution to avoid aliasing.

To further investigate the origin of the observed transport fluctuations, the spectra of the geopotential anomaly ϕ and bottom pressure at Sites A and B calculated in the same manner are also shown (Figures 6d and 6e). Both ϕ records at Sites A and B have energy near 20 days, while ϕ at Site B exhibits a very distinctive broad peak centered near 100 days, thus indicating that density variations at Site B largely drive the variability of the absolute transport at this time scale. The 72-h low-pass-filtered records of the absolute transport and ϕ at Site B are significantly anticorrelated with 99% confidence ($r = -0.86$), implying that a linear relationship between the transport and ϕ at B explains nearly 74% of the absolute transport variance, while the 72-h low-pass-filtered records of the absolute transport and ϕ at Site A are significantly correlated with 99% confidence but the correlation decreases ($r = 0.60$). Thus, observations of the density field at Site B at 49.5°W are key to the calculation of the BC transport at this latitude, but both sites are relevant in setting the time scales of variability. The spectrum of ϕ at Site AA (at the 2,885 m isobath midway between A and B; purple curve in Figure 6d) calculated for the period 2013–2015 also exhibits a peak near 100 days, albeit weaker than at Site B. The correlation between the ϕ records at Sites AA and B is low but significant with 95% confidence ($r = 0.31$), while the correlation between ϕ records at Sites A and AA is much lower ($r = 0.11$) and not significant. The absolute transport and ϕ at Site AA are also not significantly correlated ($r = -0.21$). The ϕ variability at Sites A and B is likely to be influenced by processes such as the variability of separation of the BC from the coast (e.g., Goni et al., 2011; Olson et al., 1988), meanders in the current itself, and eddies propagating into the mooring array and interacting with or superimposing on the current (e.g., Garzoli, 1993; Meinen et al., 2017). The spectra of the bottom pressure at Sites A, AA and B have similar characteristics with an apparent common signal across the sites with noisy peaks for periods shorter than 60 days, peaking most prominently at 40–50 days, especially at Site B (Figure 6e). Strong bottom pressure variations at Site A at periods less than 200 days were also identified in Meinen et al. (2018).

In the literature, energetic short-term fluctuations (at periods of 20–50 days) have also been identified from observations of the baroclinic component of the BC transport near 37–39°S (Garzoli & Bianchi, 1987; Garzoli & Simionato, 1990). Near the continental slope, the most prominent signal observed was at 21 days, which they postulated was caused by a coastally trapped wind forced response. Garzoli and Simionato (1990) attributed the energy found in the band from 20 to 50 days to wave signals propagating at different periods with opposite directions, specifically a westward propagating wave associated with frontal displacements and an eastward propagating topographic Rossby Wave. Meinen et al. (2017) also noted large westward propagating Rossby Wave-like features within the SAMBA-West array.

The physical mechanisms responsible for the observed BC baroclinic and barotropic transport variability will be examined in a following study.

The meridional velocity measurements from the ADCP at the 411-m isobath on the upper slope (Figure 1, Table 1) provide useful insights about the flow variability and its spectral distribution up on the shelf inshore of Site A. If we assume the moored ADCP velocities are representative of the mean flow inshore of Site A (i.e., from the coast to the 1,360 m isobath) and integrate them over this domain we obtain a mean and standard deviation of -0.4 ± 2.0 Sv for the 72-h low-pass filtered record (blue line in Figure 7a). The calculated transport from the ADCP velocities is very small compared to the absolute geostrophic transport estimates in the upper 628 dbar from the PIES/CPIES between Sites A and AA and between Sites AA and B (black and gray lines, respectively, in Figure 7a). The mean moored ADCP transport value also yields much smaller southward flow than the −2.7 Sv determined as the average of the CTD snapshot sections (Section 2.2.1), furthermore randomly subsampling the ADCP velocity profiles in a way that mimics the 4 CTD section snapshot realizations for 1,000 iterations indicates that only a very low fraction of the random subsamples (about 7%) would produce a mean that is comparable to the CTD time mean of −2.7 Sv. However, the mean moored ADCP transport compares well with the time-mean approximately

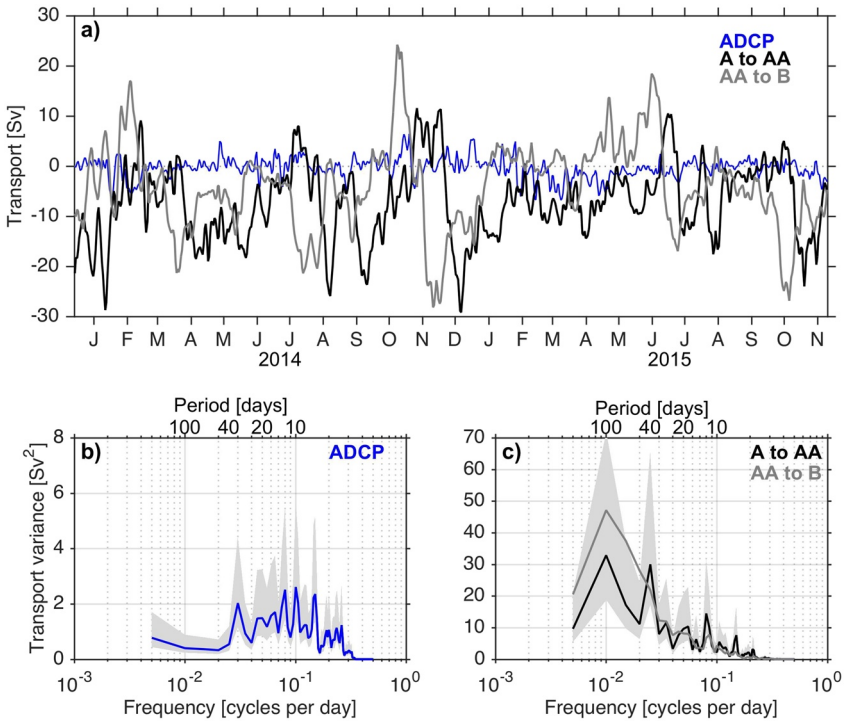

Figure 7. Transport variability on the upper continental slope. (a) Estimated 72-h low-pass filtered transport from the ADCP deployed at the 411-m isobath integrated over the area inshore of Site A (blue). Also shown are the 72-h low-pass filtered PIES/CPIES-derived absolute geostrophic transports between Sites A and AA (black) and between Sites AA and B (gray) during 2014–2015 when the ADCP and CPIES at Site AA measurements overlapped. (b) Variance preserving spectrum of daily 72-h low-pass filtered ADCP-derived transport. Shaded confidence interval (95%) is also shown. (c) Variance preserving spectrum of 72-h low-pass filtered PIES/CPIES-derived absolute geostrophic transports between Sites A and AA (black) and between Sites AA and B (gray; shaded confidence interval is not shown for clarity) during 2014–2015. Note the different scale on the *y*-axes for (b) and (c). The spectra are computed based on Welch's periodogram method using 200-day-wide Hamming window and 100-day of overlap between consecutive data segments. CPIES, current- and pressure-recording inverted echo sounder; ADCP, Acoustic Doppler Current Profiler; PIES, pressure-recording inverted echo sounder.

−0.4 to 0.3 Sv seasonally reversing flow at the shallow wide shelf from models (Palma et al., 2008). Additionally, while it is difficult to know for certain how representative the moored ADCP velocity is for the region inshore of Site A, we can definitely note that the largest portion of the variance (70%) in the ADCP record is associated with periods shorter than 40 days (Figure 7b; the spectra is calculated via Welch's periodogram method using a 200-day-wide Hamming window allowing 100 days of overlap), which seems likely to be unrelated to the BC transport variability, as the latter has a very prominent spectral peak near 100 days (Figure 6a).

The ADCP record is short and perhaps a longer record would be able to reveal more pronounced variability on time scales longer than 40 days. However, we note that spectra of the BC transport records between Sites A-AA and AA-B for the identical time period as the ADCP record, 2014–2015 (Figure 7c), are able to show a clear peak at 100 days suggesting that different dynamics are governing the flow at the shelf/upper continental slope and in the BC region.

Given the roughly 6-year length of our *in situ* transport records, estimates of the seasonal cycle and/or interannual variations can be made, with the understanding that the number of degrees of freedom is quite small. The annual climatology (average of each transport as a function of year day) of the observed 30-day low-pass filtered transports from SAMBA-West does not indicate a clear annual cycle for the period 2009–2015 for the absolute, baroclinic or barotropic components (Figure 8). The absolute and baroclinic transports exhibit very similar characteristics and amplitudes (Figures 8a and 8b), while the amplitude for the barotropic transport is much smaller (Figure 8c).

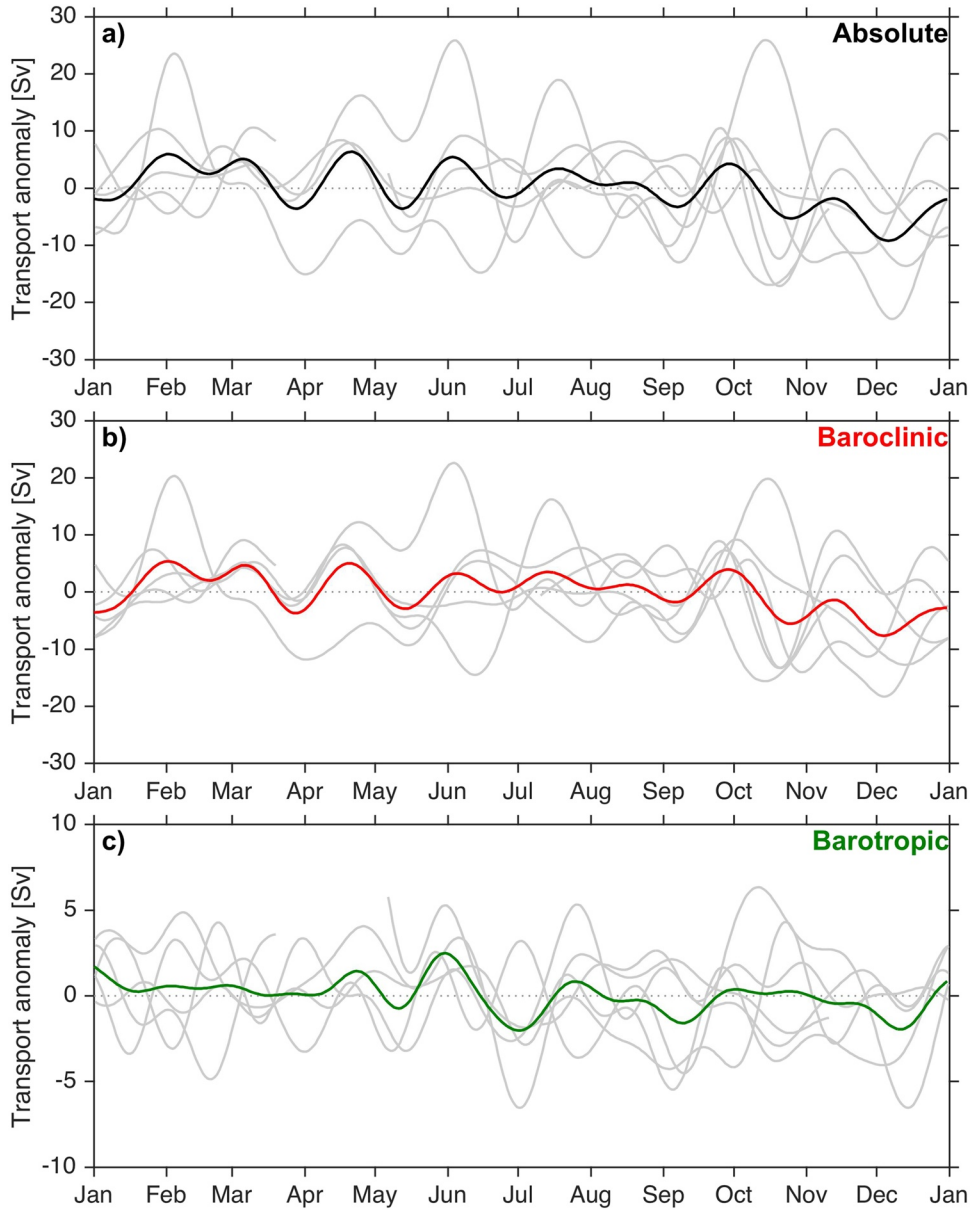

Figure 8. Annual climatology (average for each year day) of 30-day low-pass filtered (a) absolute, (b) baroclinic, and (c) barotropic Brazil Current transport anomalies. Transport anomalies are computed relative to the record-length mean. Light gray lines represent transport anomalies for each individual year; the thick black, red, and green lines are the temporal averages of all individual years in (a), (b), and (c), respectively. Note the different scale on the *y*-axes for (c). Negative values indicate southward flow anomaly.

Our measurements show the strongest southward flow anomalies toward the end of the year in November–December, and the weakest southward flow anomalies during the first half of the year. Given the large high-frequency variability of the geostrophic component of the BC transport, its seasonality does not emerge from 6 years of continuous-in-time data, note the strong northward flow anomaly in October 2014 (strong anomaly in gray line in Figures 8a–8c; see also Figure 5 and Table 4) when the seasonal cycle is shifting toward stronger southward transport anomalies (black and red curves in Figures 8a and 8b). The main difference among the three records occurs during January and July. During January, the three records have small amplitudes however both the absolute and baroclinic transport exhibit southward flow anomalies while the barotropic transport exhibits northward flow anomalies. For the period centered at the beginning of July the barotropic transport exhibits its largest southward flow anomalies, while the baroclinic transport have

near zero or northward flow anomalies. If we estimate the seasonal cycle instead as monthly means, we similarly find no clear seasonal signal, with monthly values in the absolute transport anomalies that are not statistically different from zero or from each other at even the 67% confidence level (not shown). The seasonal cycle of the BC has previously been analyzed using XBTs (Dong et al., 2014; Goes et al., 2019), as well as with synthetic products derived from Argo data, satellite altimetry, winds, and with numerical models (e.g., Combes & Matano, 2014; Matano, 1993; Schmid & Majumder, 2018). These studies consistently found a seasonal cycle with the BC intensifying during austral summer (January, February, and March) and weakening during austral winter (June, July, and August) at 35°S, consistent with the meridional displacements of the BMC at seasonal time scales (Garzoli & Bianchi, 1987; Garzoli & Garraffo, 1989; Goni & Wainer, 2001; Lumpkin & Garzoli, 2011; Olson et al., 1988; Saraceno et al., 2004) associated with the seasonal variability of the basin-wide wind stress curl (e.g., Matano et al., 1993) or with the first mode of variability of the wind stress curl in a smaller domain in the western South Atlantic (Combes & Matano, 2014). However, we find that the directly locally forced Ekman transport in the BC region at 34.5°S is very weak, and it has a very small temporal mean and standard deviation of -0.002 ± 0.225 Sv during 2009–2015 (not shown). As in previous studies the Ekman transport anomaly has a well-defined seasonal cycle at this latitude, which reaches its maximum (positive) transport in austral winter and reaches its minimum (negative) transport in austral summer (e.g., Dong et al., 2014). Thus, the Ekman component of the BC transport (computed for the BC region) has a clear seasonality, but it is very weak (peak-to-peak amplitude of only ∼0.16 Sv) compared to the much larger monthly peak-to-peak BC geostrophic transport amplitude of ∼9 Sv. The standard deviation of the Ekman transport (of 0.225 Sv) is well below the scale of the standard deviation of the observed absolute or baroclinic transport signals (of 8.8 and 7.6 Sv, respectively) indicating that the observed geostrophic transport fluctuations cannot be caused by locally forced changes induced by wind stress variability at any time scale. As a result, the annual climatology of the geostrophic absolute or baroclinic transports with the addition of the Ekman transport component yield similar results as in Figures 8a and 8b, respectively (not shown). Furthermore, there is a good correspondence between the calculated annual cycle of the BC and the DWBC below (Meinen et al., 2017), which is perhaps not surprising given the low shear between the two southward flows (e.g., Figure 4e). However, neither the BC or the DWBC show a meaningful annual cycle signal, possibly as a result of the aliasing of much stronger amplitude high frequency "noise" when attempting to extract the seasonal cycle. These results, combined with the low percent variance of absolute BC transport signals with periods longer than 150 days in Table 4, reveal that it is likely that more years of continuous measurements are needed to determine whether a robust seasonal cycle exists.

The annual means of the transport records for each individual year are given in Table 3. Note that years 2010 and 2011 have only 3 and 6 months of data, respectively, and hence are excluded from this analysis. Years 2009 and 2015 have eight and 10 months of data, respectively, and were judged usable for this analyses. During years 2009, 2012, and 2013, the annual mean absolute transport is markedly steady with only small variations compared to the record-length time-mean value of −14.0 Sv (−14.0, −14.7, and −14.8 Sv, respectively). During 2014 the strongest southward flow is observed (−16.2 Sv) and during 2015 the weakest southward flow is observed (−10.8 Sv), differing from the time-mean by −2.2 Sv (stronger southward flow, due to enhanced southward baroclinic transport, Table 3) and 3.2 Sv (weaker southward flow, due to weaker baroclinic and barotropic transport, Table 3), respectively. However, the 95% confidence limits of the annual means calculated as 2*SEM for each year-long segment are large (SEM is ∼3.0 Sv in 2014 and 2015). Additionally, fitting a linear temporal trend to the absolute BC transport for the longest continuous segment (2011–2015) yields 0.08 ± 1.78 Sv/year (-0.05 ± 1.52 Sv/year and 0.13 ± 0.57 Sv/year for the baroclinic and barotropic transports, respectively), not statistically significant with 95% confidence for 64 DOFs following the methods of Bendat and Piersol (1986). Thus, there is no statistically significant trend or deviations from the long-term mean in the yearly averages between 2009 and 2015.

To investigate the accuracy to which the monthly means and annual means can be estimated from the available 6+ years long BC transport record, we estimate the errors in monthly and annual means performing a Monte Carlo-style analysis (e.g., Emery & Thomson, 2001; Meinen et al., 2010). For the monthly averaging, we randomly selected a month from the transport time series and then we randomly subsampled estimates of daily observations within that chosen month. Subsamples ranging from one to 20 days were averaged and the root-mean-square (RMS) error was computed between those averages and the average from the complete month. A similar procedure is applied to obtain the RMS error of the annual mean estimates. The results for

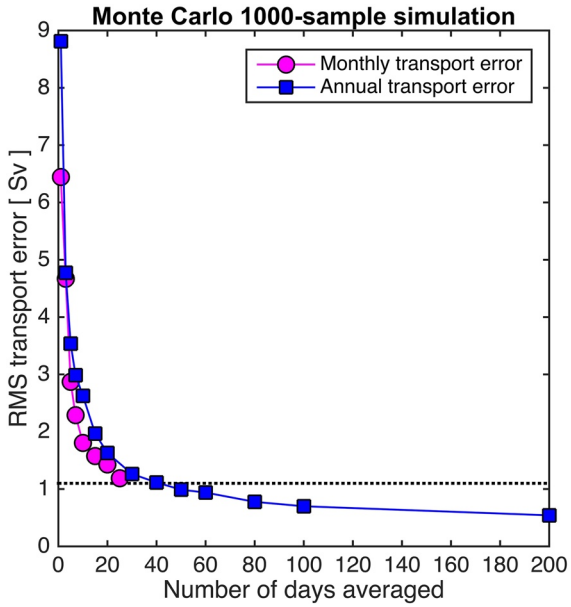

Figure 9. Root-mean-square (RMS) error in the estimates of monthly (magenta) and annual (blue) mean absolute Brazil Current transport versus number of samples considered, after a Monte Carlo-style analysis with 1,000 iterations. The horizontal dotted line indicates the Standard Error of the Mean (SEM) for the absolute transport record (1.1 Sv; Appendix A). RMS, Root-mean-square; SEM, Standard Error of the Mean.

1,000 iterations (Figure 9) indicate that, to consistently obtain a monthly value accurate to within one SEM (of 1.1 Sv, Appendix A) at least 25 daily observations within that month are needed. In order to obtain an annual mean value accurate to 1.1 Sv (or better), at least 50 randomly sub-sampled daily observations are required during that year. These results again point to the need of continuous-in-time daily measurements to resolve monthly to interannual time scales in the BC transport.

4. Summary and Conclusions

The absolute Brazil Current (BC) transport at 34.5°S, integrated between the sea-surface and the mean-pressure of the density interface between TW/SACW and AAIW, during 2009–2015 has a mean strength of −14.0 Sv, a large standard deviation of 8.8 Sv, and a large peak-to-peak range of 61.7 Sv. Transport variations of 20–30 Sv occur in periods as short as 2–3 weeks and larger variations of about 40–60 Sv occur in periods of 30–60 days, illustrating the dynamic short-term variability in the record and the necessity of continuous-in-time daily observations to avoid aliasing. The daily transport values for the BC are estimated to be accurate to within 2.8 Sv (Appendix A). The long-term PIES/CPIES array at 34.5°S has been shown to capture the majority of the variability of the BC, centered mainly in the area between 51.5°W and 49.5°W. High-resolution hydrographic section data have been used to estimate the mean related transports near the shelf/shelf-break to the west of 51.5°W (which are not currently sampled by the PIES/CPIES array) and data form a bottom moored ADCP provided important insights about upper slope and shelf velocities. Our results indicate that additional time series observations at the shelf-break between the 500 and 1,000 dbar isobaths would improve the overall estimation of the BC transport by the array. A new CPIES was deployed in mid-2019 west of PIES A at 875 m (Site 0A) and funding has been awarded to deploy a tall dynamic height mooring additionally equipped with current meters and biogeochemical sensors at the western boundary wedge currently not sampled by the PIES/CPIES array.

The results presented here reveal that the largest part of the variance (~80%) in the absolute BC transport is concentrated at periods shorter than 150 days. The spectral distribution of energy has a well-defined peak near 100 days and secondary (and noisier) peaks between 20-50 days, consistent with earlier studies of the DWBC at this same location (e.g., Meinen et al., 2017). The baroclinic component of the BC transport accounts for the largest fraction of the absolute transport variance (85%), but the barotropic variance contribution (15%) is not negligible. The baroclinic and barotropic transports are uncorrelated on a daily basis, and are only marginally correlated after smoothing with a 30-day low-pass filter. This highlights the need to measure both transport components independently in order to accurately describe the flow variability. No statistically significant seasonal cycle is found and there is no statistically significant trend or variability in the annual averages during the 6+ years of measurements. Our analyses demonstrate that to consistently obtain a monthly value accurate to within 1.1 Sv (one standard error level) at least 25 daily observations within that month are needed, and at least 50 randomly sub-sampled observations throughout a year are required to obtain an annual mean value accurate to 1.1 Sv (or better). It is likely that more years of measurements are necessary to clearly detect significant longer period (seasonal to interannual) signals and trends given the large amplitude of the variability on short time scales.

Overall, the results presented here strongly highlight the strength of a continuous observing system to capture the variability of the BC transport at subseasonal, seasonal, and interannual time scales. A future study will address the physical mechanisms that drive the meridional volume transport fluctuations observed here.

Appendix A: Error Analysis

Transport Accuracy Estimates

The transport accuracy estimates closely follow the methods in Meinen et al. (2013). The sources of the transport errors are classified as random or potential bias respective to the time variability. A detailed explanation of the sources of each error is given in Meinen et al. (2013), here we focus on the specifics of the BC estimate.

There are several sources of uncertainty that affect the τ accuracy estimated from PIES/CPIES. To convert the τ accuracies into transport accuracies, we use the linear relationship between the baroclinic streamfunction (a.k.a. Fofonoff potential or potential energy anomaly, χ) and τ at 1,000 dbar (τ_{1000}). Here, the vertical integration domain for χ is chosen to be consistent with the layer occupied by the BC (i.e., between the surface and approximately 628 dbar, $\chi^{(0-628)}$). There is a tight relationship between τ and $\chi^{(0-628)}$. The slope for a linear fit is $-0.6\ 10^5$ J m^{-2} ms^{-1}. The χ accuracy is converted into transport error bars by using the local Coriolis parameter $f = -8.2605\ 10^{-5}$ s^{-1} and a constant density of 1,030 kg m^{-3}.

The random sources of the geostrophic velocity or transport (baroclinic relative to an assumed level of no motion and barotropic or reference velocity) affect the time-variability of the transport and can be listed as follows: (1) the accuracy of PIES/CPIES-measured τ (0.17 ms; following Chidichimo et al., 2014, revised after Donohue et al., 2010); (2) the scatter in the calibration relationship to convert PIES/CPIES τ actual depth on the fixed 1,000 dbar level (0.2 ms or 0.5 Sv; as estimated in Meinen et al., 2013); (3) the accuracy of the GEM lookup tables calculated as the rms scatter about the fit between $\chi^{(0-628)}$ and τ_{1000} ($1.65\ 10^5$ J m^{-2}); (4) additionally, for the calculation of the reference velocity accuracy the sole random source of error are the pressure gauges (0.01 dbar; Donohue et al., 2010). These four random errors amount to 1.9, 0.5, 1.8, and 0.7 Sv, respectively (independent of one another) and are combined via the square-root of the sum of the squares method yielding a total random error of 2.8 Sv for the 72-h low-pass filtered BC absolute transport estimates.

There are two potential sources of bias errors affecting the time-mean transport: (1) the offset due to the calibration of τ into the equivalent τ_{index} from CTDs (1.8 ms or 1.9 Sv from Meinen et al., 2013); (2) the accuracy of the time-mean reference velocity between Sites A and B, estimated conservatively as the difference of time-mean reference velocity at 1,500 dbar between two sources: the 35-year run of OFES (1980–2015) described herein (-0.058 m s^{-1}) and a 26-year run (1992–2018) of the Estimating the Circulation and Climate of the Ocean, Phase 2 (ECCO2) ocean state estimate (https://ecco.jpl.nasa.gov/) (-0.027 m s^{-1}). The approximate difference between these estimates amount to 0.031 m s^{-1}, which considering a width of 1.8315×10^5 m and a vertical layer of about 628 m translates into a potential transport bias error of 3.5 Sv. Adding more models would refine/reduce the estimate of this source of bias in the future, but this is beyond the scope of this study. As these potential bias sources of errors are independent of one another, they are also combined via the square-root of the sum of the squares, yielding 3.9 Sv.

Degrees of Freedom, Integral Time Scales, Standard Error of the Mean

The integral time scale (ITS) for the absolute transport record is determined by the first zero crossing of the autocorrelation function of the daily transport time series (Emery & Thomson, 2001). Evaluating the longest segment with continuous measurements (between July 2011 and November 2015, almost 4.5 years of data) of the absolute transport record, results in an ITS of 12 days, thus every 24 days there is an independent "degree of freedom" (DOF) for estimating both the average and the statistical accuracy of the average. This yields about 64 DOFs and a Standard Error of the Mean (SEM) of 1.1 Sv. If we also include the first 1-year segment in the analysis, the DOFs increase to 76 and the resulting SEM is 1.0 Sv. To be conservative we keep the estimate for the longest period with continuous measurements. The ITS after applying a 30-day low-pass filter is slightly longer (14 days), thus the time series have fewer DOFs (56). The statistical significance of the correlation coefficients is calculated following the methodology described in Emery and Thomson (2001). For 60 DOFs, correlations (r) for 72-h low pass filtered records with cutoff $r = |0.250|$ and $r = |0.325|$ are significantly different from zero at the 95% and the 99% confidence level, respectively. For 50

Acknowledgments
The authors would like to thank the crews of Puerto Deseado and Ice Lady Patagonia II (Argentina), Alpha-Crucis, Alpha-Delphini and Cruzeiro do Sul (Brazil), who have supported the research cruises. Thanks also to the support/technical teams in Miami, São Paulo, Buenos Aires, who have helped collect and process the data presented herein. M. Charo, R. Guerrero, D. Valla, C. França, R. Garcia, P. Peña, and U. Rivero are gratefully acknowledged for their invaluable work with the collection and calibration of the hydrographic and PIES data used in this study. The SAMBA-West hydrographic observations and the participation of M. P. Chidichimo and A. Piola were supported by funds from Servicio de Hidrografía Naval, CONICET, NOAA, and the Inter-American Institute for Global Change Research grants CRN2076 and CRN3070, through the U. S. National Science Foundation grants GEO-0452325 and GEO-1128040. The U.S. PIES observations and the participation of C. Meinen, R. Perez, S. Dong, and S. Garzoli were supported via the NOAA Global Ocean Monitoring and Observing program (FundRef# 100007298) under the Southwest Atlantic Meridional Overturning Circulation ("SAM") project. The Brazilian CPIES and ADCP observations and the participation of E. Campos were supported by CNPq (Grant 302503/2019-6) and FAPESP through projects SAMOC (Grant 2011/50552-4) and SAMBAR (Grant 2017/09659-6).
M. P. Chidichimo and A. Piola also acknowledge funding support from the European Union's Horizon 2020 Research and Innovation Program under grant agreement no. 818123 (iAtlantic). C. Meinen, R. Perez, S. Dong, R. Lumpkin, S. Garzoli also acknowledge additional support from the NOAA Atlantic Oceanographic and Meteorological Laboratory. C. Meinen and R. Perez acknowledge additional support from NOAA Climate Variability Program (GC16-212). R. Perez and S. Garzoli acknowledge additional support from NOAA (grant NA13OAR4310131) and NASA (grant NNX14AH60G). SD acknowledge additional support from NOAA Climate Variability Program (GC16-210) and NOAA Global Ocean Monitoring and Observing program under the XBT project and State of the Climate: Quarterly Report on the Meridional Heat Transport in the Atlantic Ocean project. Thanks to D. Volkov for providing the run from the Estimating the Circulation and Climate of the Ocean, Phase 2 (ECCO2) ocean state estimate (https://ecco.jpl.nasa.gov/). The authors are very grateful for the constructive comments by two anonymous reviewers.

DOFs, correlations with cutoff $r = |0.273|$ and $r = |0.354|$ are significantly different from zero at the 95% and the 99% confidence level, respectively.

Data Availability Statement

The PIES/CPIES and hydrographic data used herein from the South Atlantic MOC Basin-wide Array (SAMBA) can be found at: https://www.aoml.noaa.gov/phod/SAMOC_international/samoc_data.php. The STSF hydrographic and LADCP data are available at https://doi.org/10.7910/DVN/IHWLL3 and https://doi.org/10.7910/DVN/JJNFKG, respectively.

References

Ansorge, I. J., Baringer, M. O., Campos, E. J. D., Dong, S., Fine, R. A., Garzoli, S. L., et al. (2014). Basin-wide oceanographic array bridges the South Atlantic. *Eos Transactions American Geophysical Union*, *95*(6), 53–54. https://doi.org/10.1002/2014EO060001

Archer, M. R., Keating, S. R., Roughan, M., Johns, W. E., Lumpkin, R., Beron-Vera, F. J., & Shay, L. K. (2018). The kinematic similarity of two western boundary currents revealed by sustained high-resolution observations. *Geophysical Research Letters*, *45*. https://doi.org/10.1029/2018GL078429

Bendat, J. S., & Piersol, A. G. (1986). Random data: Analysis and measurement procedures (2nd ed.). New York: Wiley Interscience. 566 pp.

Berden, G., Charo, M., Möller, O. O., & Piola, A. R. (2020). Circulation and hydrography in the western south atlantic shelf and export to the deep adjacent ocean: 30°S to 40°S. *Journal of Geophysical Research: Oceans*, *125*, e2020JC016500. https://doi.org/10.1029/2020JC016500

Biastoch, A., Böning, C. W., & Lutjeharms, J. R. E. (2008). Agulhas leakage dynamics affects decadal variability in atlantic overturning circulation. *Nature*, *456*, 489–492. https://doi.org/10.1038/nature07426

Biló, T. C., da Silveira, I. C. A., Belo, W. C., de Castro, B. M., & Piola, A. R. (2014). Methods for estimating the velocities of the Brazil Current in the pre-salt reservoir area off southeast Brazil (23° S–26° S). *Ocean Dynamics*, *64*(10), 1431–1446. https://doi.org/10.1007/s10236-014-0761-2

Bishop, S. P., Watts, D. R., Park, J.-H., & Hogg, N. G. (2012). Evidence of bottom-trapped currents in the Kuroshio Extension region. *Journal of Physical Oceanography*, *42*(2), 321–328. https://doi.org/10.1175/JPO-D-11-0144.1

Boebel, O., Davis, R. E., Ollitrault, M., Peterson, R. G., Richardson, P. L., Schmid, C., & Zenk, W. (1999). The intermediate depth circulation of the western South Atlantic. *Geophysical Research Letters*, *26*, 3329–3332. https://doi.org/10.1029/1999GL002355

Bryden, H. L., King, B. A., & McCarthy, G. D. (2011). South Atlantic overturning circulation at 24°S. *Journal of Marine Research*, *69*(1), 38–55. https://doi.org/10.1357/002224011798147633

Calado, L., Da Silveira, I. C. A., Gangopadhyay, A., & De Castro, B. M. (2010). Eddy-induced upwelling off Cape São Tomé (22°S, Brazil). *Continental Shelf Research*, *30*(10–11), 1181–1188. https://doi.org/10.1016/j.csr.2010.03.007

Campos, E. J. D., Gonçalves, J. E., & Ikeda, Y. (1995). Water mass characteristics and geostrophic circulation in the South Brazil Bight: Summer of 1991. *Journal of Geophysical Research*, *100*(C9), 18537–18550. https://doi.org/10.1029/95JC01724

Campos, E. J. D., Velhote, D., & da Silveira, I. C. A. (2000). Shelf break upwelling driven by Brazil Current cyclonic meanders. *Geophysical Research Letters*, *27*(6), 751–754. https://doi.org/10.1029/1999GL010502

Charo, M., Guerrero, R., & Piola, A. (2020). Subtropical shelf front cruise – conductivity-temperature-depth (CTD) data. Harvard Dataverse, V1 https://doi.org/10.7910/DVN/IHWLL3

Charo, M., Valla, D., Fenco, H., & Piola, A. (2020). Subtropical shelf front cruise – lowered acoustic Doppler profiler. Harvard Dataverse, V1 (LADCP) data, https://doi.org/10.7910/DVN/JJNFKG

Chidichimo, M. P., Donohue, K. A., Watts, D. R., & Tracey, K. L. (2014). Baroclinic transport time series of the Antarctic Circumpolar Current measured in Drake Passage. *Journal of Physical Oceanography*, *44*(7), 1829–1853. https://doi.org/10.1175/JPO-D-13-071.1

Combes, V., & Matano, R. P. (2014). A two-way nested simulation of the oceanic circulation in the Southwestern Atlantic. *Journal of Geophysical Research: Oceans*, *119*(2), 731–756. https://doi.org/10.1002/2013JC009498

Confluence Principal Investigators. (1990). CONFLUENCE 1988-1990: An intensive study of the southwestern Atlantic. *Eos Transactions American Geophysical Union*, *71*(41), 1131–1133. https://doi.org/10.1029/90EO00313

Côté, J. M., Hotchkiss, F. S., Martini, M., & Denham, C. R. (2011). Acoustic Doppler Current Profiler (ADCP) data processing system manual: U.S. Geological Survey Open File Report 00-458, v. *4*, 51 p.

de Souza, M. M., Mathis, M., & Pohlmann, T. (2019). Driving mechanisms of the variability and long-term trend of the Brazil-Malvinas confluence during the 21st century. *Climate Dynamics*, *53*, 6453–6468. https://doi.org/10.1007/s00382-019-04942-7

Dijkstra, H. A. (2007). Characterization of the multiple equilibria regime in a global ocean model. *Tellus A: Dynamic Meteorology and Oceanography*, *59*, 695–705. https://doi.org/10.1111/j.1600-0870.2007.00267.x

Dong, S., Baringer, M., Goni, G., & Garzoli, S. (2011). Importance of the assimilation of Argo Float Measurements on the Meridional Overturning Circulation in the South Atlantic. *Geophysical Research Letters*, *38*, L18603. https://doi.org/10.1029/2011GL048982

Dong, S., Baringer, M. O., Goni, G. J., Meinen, C. S., & Garzoli, S. L. (2014). Seasonal variations in the South Atlantic Meridional Overturning Circulation from observations and numerical models. *Geophysical Research Letters*, *41*, 4611. https://doi.org/10.1002/2014GL060428

Dong, S., Garzoli, S., Baringer, M., Meinen, C., & Goni, G. (2009). Interannual variations in the Atlantic meridional overturning circulation and its relationship with the net northward heat transport in the South Atlantic. *Geophysical Research Letters*, *36*, L20606. https://doi.org/10.1029/2009GL039356

Dong, S., Garzoli, S. L., & Baringer, M. O. (2011b). The role of interocean exchanges on decadal variations of the northward heat transport in the South Atlantic. *Journal of Physical Oceanography*, *41*(8), 1498–1511. https://doi.org/10.1175/2011JPO4549.1

Dong, S., Goni, G., & Bringas, F. (2015). Temporal variability of the South Atlantic Meridional Overturning Circulation between 20°S and 35°S. *Geophysical Research Letters*, *42*, 7655–7662. https://doi.org/10.1002/2015GL065603

Donohue, K. A., Watts, D. R., Tracey, K. L., Greene, A. D., & Kennelly, M. (2010). Mapping circulation in the Kuroshio Extension with an array of current and pressure recording inverted echo sounders. *Journal of Atmospheric and Oceanic Technology*, *27*, 507–527. https://doi.org/10.1175/2009JTECHO686.1

Drifjhout, S. S., Weber, S. L., & van der Swaluw, E. (2011). The stability of the MOC as diagnosed from model projections for pre-industrial, present and future climates. *Climate Dynamics*, *37*(7), 1575–1586. https://doi.org/10.1007/s00382-010-0930-z

Drouin, K. L., Lozier, M. S., & Johns, W. E. (2021). Variability and trends of the South Atlantic subtropical gyre. *Journal of Geophysical Research: Oceans*, *126*. https://doi.org/10.1029/2020jc016405

Emery, W. J., & Thomson, R. E. (2001). Data analysis methods in physical oceanography. In W. J. Emery, & R. E. Thomson (Eds.), p. 654. Amsterdam: Elsevier Science. https://doi.org/10.1016/B978-0-444-50756-3.X5000-X

Ferrari, R., Artana, C., Saraceno, M., Piola, A. R., & Provost, C. (2017). Satellite altimetry and current-meter velocities in the malvinas current at 41°S: Comparisons and modes of variations. *Journal of Geophysical Research: Oceans*, *122*, 9572–9590. https://doi.org/10.1002/2017JC013340

Frajka-Williams, E., Ansorge, I. J., Baehr, J., Bryden, H. L., Chidichimo, M. P., Cunningham, S. A., et al. (2019). Atlantic Meridional Overturning Circulation: Observed transports and variability. *Frontiers in Marine Science*, *6*, 260. https://doi.org/10.3389/fmars.2019.00260

Garfield, N., III (1990). The Brazil Current at subtropical latitudes. Ph.D thesis, 121 pp., Kingston, RI: University of Rhode Island.

Garzoli, S., Abrahamsen, P., Ansorge, I., Biastoch, A., Campos, E., Mata, M., et al. (2012). South Atlantic Meridional Overturning Circulation (SAMOC) – Fourth Workshop. *CLIVAR Exchanges*, *58*, 2–4.

Garzoli, S., & Simionato, C. (1990). Baroclinic instabilities and forced oscillations in the Brazil/Malvinas confluence front. *Deep-Sea Research Part A. Oceanographic Research Papers*, *37*(6), 1053–1074. https://doi.org/10.1016/0198-0149(90)90110-H

Garzoli, S. L. (1993). Geostrophic velocity and transport variability in the Brazil-Malvinas confluence. *Deep Sea Research Part I: Oceanographic Research Papers*, *40*(7), 1379–1403. http://doi.org/10.1016/0967-0637(93)90118-M

Garzoli, S. L., & Baringer, M. O. (2007). Meridional heat transport determined with expandable bathythermographs–Part II: South Atlantic transport. *Deep Sea Research Part I: Oceanographic Research Papers*, *54*, 1402–1420. https://doi.org/10.1016/j.dsr.2007.04.013

Garzoli, S. L., Baringer, M. O., Dong, S., Perez, R. C., & Yao, Q. (2013). South Atlantic meridional fluxes. *Deep Sea Research Part I: Oceanographic Research Papers*, *71*, 21–32. https://doi.org/10.1016/j.dsr.2012.09.003. http://doi.org/10.1016/j.dsr.2012.09.003

Garzoli, S. L., & Bianchi, A. (1987). Time-space variability of the local dynamics of the Malvinas-Brazil confluence as revealed by inverted echo sounders. *Journal of Geophysical Research*, *92*(C2), 1914–1922. https://doi.org/10.1029/JC092iC02p01914

Garzoli, S. L., & Garraffo, Z. (1989). Transports, frontal motions and eddies at the Brazil-Malvinas currents confluence. *Deep-Sea Research Part A. Oceanographic Research Papers*, *36*(5), 681–703. https://doi.org/10.1016/0198-0149(89)90145-3 ISSN 0198-0149.

Garzoli, S. L., & Matano, R. (2011). The south atlantic and the atlantic meridional overturning circulation. *Deep Sea Research Part II: Topical Studies in Oceanography*, *58*(17–18), 1837–1847, https://doi.org/10.1016/j.dsr2.2010.10.063

Gill, A. (1982). Atmosphere-ocean dynamics. International Geophysics Series (1st ed.), 30, p. 662. London, UK: Academic Press 9780122835223.

Goes, M., Cirano, M., Mata, M. M., & Majumder, S. (2019). Long-term monitoring of the Brazil current transport at 22°s from XBT and altimetry data: Seasonal, interannual, and extreme variability. *Journal of Geophysical Research: Oceans*, *124*, 3645–3663. https://doi.org/10.1029/2018JC014809

Goni, G., Kamholz, S., Garzoli, S., & Olson, D. (1996). Dynamics of the Brazil-Malvinas Confluence based on inverted echo sounders and altimetry. *Journal of Geophysical Research*, *101*(C7), 16273–16289. https://doi.org/10.1029/96jc01146

Goni, G. J., Bringas, F., & DiNezio, P. N. (2011). Observed low frequency variability of the Brazil Current front. *Journal of Geophysical Research*, *116*(C10), c10037. https://doi.org/10.1029/2011JC007198

Goni, G. J., & Wainer, I. (2001). Investigation of the Brazil Current front variability from altimeter data. *Journal of Geophysical Research*, *106*(C12), 31117–31128. https://doi.org/10.1029/2000JC000396

Gordon, A. L., & Greengrove, C. L. (1986). Geostrophic circulation of the Brazil-Falkland confluence. *Deep-Sea Research Part A. Oceanographic Research Papers*, *33*(5), 573–585. https://doi.org/10.1016/0198-0149(86)90054-3

Greene, A. D., Watts, D. R., Sutyrin, G. G., & Sasaki, H. (2012). Evidence of Vertical Coupling between the Kuroshio Extension and Topographically Controlled Deep Eddies. *Journal of Marine Research*, *70*, 719–747. https://doi.org/10.1357/002224012806290723

Herrford, J., Brandt, P., Kanzow, T., Hummels, R., Araujo, M., & Durgadoo, J. V. (2021). Seasonal variability of the Atlantic Meridional Overturning Circulation at 11°S inferred from bottom pressure measurements. *Ocean Science*, *17*, 265–284, 2021. https://doi.org/10.5194/os-17-265-2021

Huisman, S. E., den Toom, M., Dijkstra, H. A., & Drijfhout, S. (2010). An indicator of the multiple equilibria regime of the atlantic meridional overturning circulation. *Journal of Physical Oceanography*, *40*(3), 551–567. https://doi.org/10.1175/2009JPO4215.1

Hummels, R., Brandt, P., Dengler, M., Fischer, J., Araujo, M., Veleda, D., & Durgadoo, J. V. (2015). Interannual to decadal changes in the western boundary circulation in the Atlantic at 11°S. *Geophysical Research Letters*, *42*, 7615–7622. https://doi.org/10.1002/2015GL065254

Imawaki, S., Bower, A., Beal, L., & Qiu, B. (2013). Western boundary currents. In G. Siedler, S. M. Griffies, J. Gould, & J. A. Church (Eds.), in *Ocean circulation and climate – a 21st century perspective* (pp. 305–338). Amsterdam: Elsevier Academic Press. https://doi.org/10.1016/B978-0-12-391851-2.00013-1

Jackett, D. R., & McDougall, T. J. (1997). A neutral density variable for the world's oceans. *Journal of Physical Oceanography*, *27*(2), 237–263. https://doi.org/10.1175/1520-0485(1997)027<0237:andvft>2.0.co;2. Retrieved Dec 28, 2020, from https://journals.ametsoc.org/view/journals/phoc/27/2/1520-0485_1997_027_0237_andvft_2.0.co_2.xml

Kersalé, M., Meinen, C. S., Perez, R. C., Le Hénaff, M., Valla, D., Lamont, T., et al. (2020). Highly Variable Upper and Abyssal Overturning Cells in the South Atlantic. *Science Advances*, *6*(32), eaba7573. https://doi.org/10.1126/sciadv.aba7573

Kersalé, M., Perez, R. C., Speich, S., Meinen, C. S., Lamont, T., Le Hénaff, M., et al. (2019). Shallow and deep eastern boundary currents in the South Atlantic at 34.5°S: Mean structure and variability. *Journal of Geophysical Research: Oceans*, *124*, 1634– 1659. https://doi.org/10.1029/2018JC014554

King, B. A., & Hamersley, D. R. C. (2010). RRS James Cook cruise JC032, 07 March to 21 April 2009. Hydrographic sections accross the Brazil current and at 24°S in the Atlantic, p. 173. Southampton, UK: National Oceanographic Centre Southampton.

Lima, M. O., Cirano, M., Mata, M. M., Goes, M., Goni, G., & Baringer, M. (2016). An assessment of the Brazil Current baroclinic structure and variability near 22° S in Distinct Ocean Forecasting and Analysis Systems. *Ocean Dynamics*, *66*(6–7), 893–916. https://doi.org/10.1007/s10236-016-0959-6

Lumpkin, R., & Garzoli, S. (2011). Interannual to decadal changes in the western South Atlantic's surface circulation. *Journal of Geophysical Research*, *116*(C1), c01014. https://doi.org/10.1029/2010JC006285

Matano, R. P., Schlax, M. G., & Chelton, D. B. (1993). Seasonal variability in the southwestern Atlantic. *Journal of Geophysical Research*, *98*(C10), 18027–18035. https://doi.org/10.1029/93JC01602

Meinen, C. S., Baringer, M. O., & Garcia, R. F. (2010). Florida Current transport variability: An analysis of annual and longer-period signals. *Deep Sea Research Part I: Oceanographic Research Papers*, *57*(7), 835–846.ISSN 0967-0637. https://doi.org/10.1016/j.dsr.2010.04.001

Meinen, C. S., Garzoli, S. L., Perez, R. C., Campos, E., Piola, A. R., Chidichimo, M. P., et al. (2017). Characteristics and causes of Deep Western Boundary Current transport variability at 34.5° S during 2009-2014. *Ocean Science*, *13*(1), 175–194. https://doi.org/10.5194/os-13-175-2017

Meinen, C. S., & Luther, D. S. (2016). Structure, transport, and vertical coherence of the gulf stream from the straits of Florida to the southeast newfoundland ridge. *Deep Sea Research Part I: Oceanographic Research Papers*, *112*, 137–154. https://doi.org/10.1016/j.dsr.2016.03.002

Meinen, C. S., Piola, A. R., Perez, R. C., & Garzoli, S. L. (2012). Deep Western Boundary Current transport variability in the South Atlantic: Preliminary results from a pilot array at 34.5°S. *Ocean Science*, *8*(6), 1041–1054. https://doi.org/10.5194/os-8-1041-2012

Meinen, C. S., Speich, S., Perez, R. C., Dong, S., Piola, A. R., Garzoli, S. L., et al. (2013). Temporal variability of the meridional overturning circulation at 34.5°S: Results from two pilot boundary arrays in the South Atlantic. *Journal of Geophysical Research: Oceans*, *118*(12), 6461–6478. https://doi.org/10.1002/2013JC009228

Meinen, C. S., Speich, S., Piola, A. R., Ansorge, I., Campos, E., Kersalé, M., et al. (2018). Meridional overturning circulation transport variability at 34.5°S during 2009–2017: Baroclinic and barotropic flows and the dueling influence of the boundaries. *Geophysical Research Letters*, *45*(9), 4180–4188. https://doi.org/10.1029/2018GL077408

Meinen, C. S., & Watts, D. R. (2000). Vertical structure and transport on a transect across the North Atlantic Current near 42°N: Time series and mean. *Journal of Geophysical Research*, *105*, 21869–21891. https://doi.org/10.1029/2000JC900097

Müller, T. J., Ikeda, Y., Zangenberg, N., & Nonato, L. V. (1998). Direct measurements of western boundary currents off Brazil between 20°S and 28°S. *Journal of Geophysical Research*, *103*(C3), 5429–5437. https://doi.org/10.1029/97JC03529

Munk, W., & Cartwright, D. (1966). Tidal spectroscopy and prediction. *Philosophical Transactions of the Royal Society of London - Series A: Mathematical and Physical Sciences 259*, 533–581. https://doi.org/10.1098/rsta.1966.0024

Oliveira, L. R., Piola, A. R., Mata, M. M., & Soares, I. D. (2009). Brazil Current surface circulation and energetics observed from drifting buoys. *Journal of Geophysical Research*, *114*, C10006. https://doi.org/10.1029/2008JC004900

Olson, D. B., Podesta, G. P., Evans, R. H., & Brown, O. B. (1988). Temporal variations in the separation of Brazil and Malvinas currents. *Deep-Sea Research Part A, Oceanographic Research Papers*, *35*(12), 1971–1990. https://doi.org/10.1016/0198-0149(88)90120-3

Palma, E. D., Matano, R. P., & Piola, A. R. (2004). A numerical study of the Southwestern Atlantic Shelf circulation: Barotropic response to tidal and wind forcing. *Journal of Geophysical Research*, *109*, C08014. https://doi.org/10.1029/2004JC002315

Palma, E. D., Matano, R. P., & Piola, A. R. (2008). A numerical study of the Southwestern Atlantic Shelf circulation: Stratified ocean response to local and offshore forcing. *Journal of Geophysical Research*, *113*(C11), c11010. https://doi.org/10.1029/2007JC004720

Palmer, M. D., Durack, P. J., Chidichimo, M. P., Church, J. A., Cravatte, S., Hill, K., et al. (2019). Adequacy of the ocean observation system for quantifying regional heat and freshwater storage and change. *Frontiers in Marine Science*, *6*, 416. https://doi.org/10.3389/fmars.2019.00416

Perez, R. C., Garzoli, S. L., Meinen, C. S., & Matano, R. P. (2011). Geostrophic Velocity Measurement Techniques for the Meridional Overturning Circulation and Meridional Heat Transport in the South Atlantic. *Journal of Atmospheric and Oceanic Technology*, *28*, 1504–1521. https://doi.org/10.1175/JTECH-D-11-00058.1

Peterson, R. G., & Stramma, L. (1991). Upper–level circulation in the South Atlantic Ocean. *Progress in Oceanography*, *26*, 1–73. https://doi.org/10.1016/0079-6611(91)90006-8

Rennell, J. (1832). Investigation of the currents of the Atlantic Ocean, and of those which prevail between the Indian ocean and the atlantic. London. Published for Lady Rodd by J.G. & F. Rivington, (OCoLC)757616581, p. 359.

Riser, S. C., Freeland, H. J., Roemmich, D., Wijffels, S., Troisi, A., Belbéoch, M., et al. (2016). Fifteen years of ocean observations with the global Argo array. *Nature Climate Change 6*, 145–153. https://doi.org/10.1038/nclimate2872

Rodrigues, R. R., Rothstein, L. M., & Wimbush, M. (2007). Seasonal variability of the South Equatorial Current bifurcation in the Atlantic Ocean: A numerical study. *Journal of Physical Oceanography*, *37*(1), 16–30. https://doi.org/10.1175/JPO2983.1

Rodrigues, R. R., Wimbush, M., Watts, D. R., Rothstein, L. M., & Ollitrault, M. (2010). South Atlantic mass transports obtained from subsurface float and hydrographic data *Journal of Marine Research*. *68*, 819–850. https://doi.org/10.1357/002224010796673858

Rossby, T. (1969). On monitoring depth variations of the main thermocline acoustically. *Journal of Geophysical Research*, *74*(23), 5542–5546. https://doi.org/10.1029/JC074i023p05542

Rühs, S., Getzlaff, K., Durgadoo, J. V., Biastoch, A., & Böning, C. W. (2015). On the suitability of North Brazil Current transport estimates for monitoring basin-scale AMOC changes. *Geophysical Research Letters*, *42*, 8072–8080. https://doi.org/10.1002/2015GL065695

Saraceno, M., Provost, C., Piola, A. R., Bava, J., & Gagliardini, A. (2004). Brazil Malvinas Frontal System as seen from 9 years of advanced very high resolution radiometer data. *Journal of Geophysical Research*, *109*, C05027. https://doi.org/10.1029/2003JC002127

Sasaki, H., Nonaka, M., Masumoto, Y., Sasai, Y., Uehara, H., & Sakuma, H. (2008). An eddy-resolving hindcast simulation of the quasiglobal ocean from 1950 to 2003 on the Earth Simulator. In *High resolution numerical modelling of the atmosphere and ocean*. (pp. 157–185). New York, NY: Springer. https://doi.org/10.1007/978-0-387-49791-4_10

Schmid, C. (2014). Mean vertical and horizontal structure of the subtropical circulation in the South Atlantic from three-dimensional observed velocity fields. *Deep Sea Research Part I: Oceanographic Research Papers*, *91*(9), 50–71. https://doi.org/10.1016/j.dsr.2014.04.015

Schmid, C., & Majumder, S. (2018). Transport variability of the Brazil Current from observations and a data assimilation model. *Ocean Science*, *14*(3), 417–436. https://doi.org/10.5194/os-14-417-2018

Smith, W. H. F., & Sandwell, D. T. (1997). Global Sea Floor Topography from Satellite Altimetry and Ship Depth Soundings. *Science*, *277*, 1956–1962. https://doi.org/10.1126/science.277.5334.1956

Soutelino, R. G., da Silveira, I. C. A., Gangopadhyay, A., & Miranda, J. A. (2011). Is the Brazil Current eddy-dominated to the north of 20°S? *Geophysical Research Letters*, *38*, L03607. https://doi.org/10.1029/2010GL046276

Spadone, A., & Provost, C. (2009). Variations in the Malvinas Current volume transport since October 1992. *Journal of Geophysical Research*, *114*, C02002. https://doi.org/10.1029/2008JC004882

Stramma, L. (1989). The Brazil current transport south of 23°S. *Deep-Sea Research Part A. Oceanographic Research Papers*, *36*, 639–646. https://doi.org/10.1016/0198-0149(89)90012-5

Stramma, L. (1991). Geostrophic transport of the South Equatorial Current in the Atlantic. *Journal of Marine Research*, *49*(2), 281–294. https://doi.org/10.1357/002224091784995864

Stramma, L., Ikeda, Y., & Peterson, R. G. (1990). Geostrophic transport in the Brazil current region north of 20°S. *Deep-Sea Research Part A. Oceanographic Research Papers*, *37*(12), 1875–1886. https://doi.org/10.1016/0198-0149(90)90083-8

Todd, R. E., Chavez, F. P., Clayton, S., Cravatte, S. E., Goes, M. P., Graco, M. I., et al. (2019). Global perspectives on observing ocean boundary current systems. *Frontiers in Marine Science*, *6*. https://doi.org/10.3389/fmars.2019.00423

Tracey, K. L., Howden, S. D., & Watts, D. R. (1997). IES Calibration and Mapping Procedures. *Journal of Atmospheric and Oceanic Technology*, *14*, 1483–1493. https://doi.org/10.1175/1520-0426(1997)014<1483:ICAMP>2.0.CO.2

Valla, D., Piola, A. R., Meinen, C. S., & Campos, E. (2018). Strong mixing and recirculation in the northwestern Argentine Basin. *Journal of Geophysical Research: Oceans*, *123*(7), 4624–4648. https://doi.org/10.1029/2018JC013907

Valla, D., Piola, A. R., Meinen, C. S., & Campos, E. (2019). Abyssal transport variations in the southwest South Atlantic: First insights from a long-term observation array at 34.5°S. *Geophysical Research Letters*, *46*(12), 6699–6705. https://doi.org/10.1029/2019GL082740

Vivier, F., & Provost, C. (1999). Direct velocity measurements in the Malvinas Current. *Journal of Geophysical Research*, *104*(C9), 21083–21103. https://doi.org/10.1029/1999JC900163

Watts, D., & Rossby, H. T. (1977). Measuring dynamic heights with inverted echo sounders: Results from MODE. *Journal of Physical Oceanography*, *7*, 345–358. https://doi.org/10.1175/1520-0485(1977)007<0345:MDHWIE>2.0.CO;2

Watts, D. R., & Kontoyiannis, H. (1990). Deep-ocean bottom pressure measurement: Drift removal and performance. *Journal of Atmospheric and Oceanic Technology*, *7*, 296–306. https://doi.org/10.1175/1520-0426(1990)007<0296:DOBPMD>2.0.CO;2

Watts, D. R., Tracey, K. L., Jr., Bane, J. M., & Shay, T. J. (1995). Gulf Stream path and thermocline structure near 74°W and 68°W. *Journal of Geophysical Research*, *100*, 18291–18312. https://doi.org/10.1029/95jc01850

Weijer, W., Cheng, W., Drijfhout, S. S., Federov, A. V., Hu, A., Jackson, L. C., et al. (2019). Stability of the Atlantic Meridional Overturning Circulation: A review and synthesis. *Journal of Geophysical Research: Oceans*, *124*. https://doi.org/10.1029/2019JC015083

Welch, P. (1967). The use of fast Fourier transform for the estimation of power spectra: A method based on time averaging over short, modified periodograms. *IEEE Transactions on Audio and Electroacoustics*, *15*(2), 70–73. https://doi.org/10.1109/tau.1967.1161901

Yang, H., Lohmann, G., Krebs-Kanzow, U., Ionita, M., Shi, X., Sidorenko, D., et al. (2020). Poleward shift of the major ocean gyres detected in a warming climate. *Geophysical Research Letters*, *47*, e2019GL085868. https://doi.org/10.1029/2019GL085868

Yang, H., Lohmann, G., Wei, W., Dima, M., Ionita, M., & Liu, J. (2016). Intensification and poleward shift of subtropical western boundary currents in a warming climate. *Journal of Geophysical Research: Oceans*, *121*, 4928–4945. https://doi.org/10.1002/2015JC011513

Zemba, J. C. (1991). The structure and transport of the Brazil Current between 27° and 36° South, Ph.D. Thesis, *Woods Hole Oceanographic Institution–Massachusetts Institute of 1331 Technology Joint Program, WHOI Technical Report 91–37*, Woods Hole Massachusetts, p. 160.